A Study on the Photospheric Polar Magnetic Patches of the Sun as Revealed with Hinode

A dissertation submitted in partial fulfillment of
the requirements for the degree of
Doctor of Philosophy

by

Anjali John Kaithakkal

Department of Astronomical Science,
School of Physical Science,
The Graduate University for Advanced Studies

Acknowledgements

First of all, I would like to thank my advisors, Associate Professor Yoshinori Suematsu, Assistant Professor Masahito Kubo and Professor Tetsuya Watanabe for their invaluable guidance and support. My special thanks to Professor Saku Tsuneta for inspiring discussions and guidance. My sincere thanks to Dr. Daikou Shiota for helping me out with IDL programming and data analysis. I also like to thank Dr. Yusuke Iida for providing me his code to use for my study.

I would like to thank Dr. Ryohko Ishikawa who was always ready to help me out with science and everyday life in Japan. My thanks to Drs. Robert Cameron, D. Orozco Suarez, Yukio Katsukawa, Takashi Sakurai, Toshifumi Shimizu, Takashi Sekii and Kiyoshi Ichimoto for useful discussions. I thank (soon to be Dr.) Nobuharu Sako and other members of the solar physics group of National Astronomical Observatory for making my stay in Japan comfortable.

Data for my study were taken from spectropolarimeter (SP) of Solar Optical Telescope (SOT) aboard Hinode satellite. Hinode is a Japanese mission developed and launched by ISAS/JAXA, collaborating with NAOJ as a domestic partner, NASA and STFC (UK) as international partners. Scientific operation of the Hinode mission is conducted by the Hinode science team organized at ISAS/JAXA. This team mainly consists of scientists from institutes in the partner countries. Support for the post-launch operation is provided by JAXA and NAOJ (Japan), STFC (UK), NASA, ESA, and NSC (Norway).

I would like to thank the Ministry of Education, Culture, Sports, Science, and Technology (MEXT) of Japan for financial support through its doctoral fellowship program for foreign students and the Graduate University for Advanced Studies (GUAS / SOKENDAI) for an associate researchers grant.

Last but not least, I am deeply grateful to my parents and siblings for their prayers, constant support and encouragement. I am very thankful that God had blessed me with such amazing people in my life.

Abstract

The distribution and evolution of the Sun′s polar magnetic field is of vital importance to understand the origin of the solar magnetism, its periodic variation and the heliospheric magnetic flux. Recent high resolution observations from the Hinode satellite have revealed that the polar region is dominated by unipolar magnetic patches which possess magnetic fields with field strengths exceeding 1 kG. The basic properties, mechanism of formation and reversal of the polar magnetic fields are topics which are yet to be resolved. Our purpose is to quantitatively study the spatial fine structure of and interaction of photospheric plasma flows with the polar magnetic patches using observations obtained with the Solar Optical Telescope (SOT) aboard the Hinode satellite. The advantage with Hinode is that, it provides unprecedented observations with high polarimetric sensitivity and spatial resolution even at higher solar latitudes.

We carried out a statistical study of the relation between polar magnetic patches and polar faculae. Polar faculae are unique because they take part in the activity cycle and their count is considered as a good proxy for the polar magnetic field. They are bright, small-scale magnetic features observed at higher heliographic latitudes. Previous studies have shown that polar faculae cycle has a periodicity of 11- years and is out-of-phase with the sunspot cycle. To obtain the correlation between polar faculae and the polar magnetic patches, we used observations of the north polar region taken in 2007 September for our study. The period of observation is close to the solar cycle minimum, and hence the polar faculae

occurrence is maximum. We found that polar faculae are enclosed within majority of the magnetic patches with flux greater than 10^{18} Mx. Magnetic patches without polar faculae dominate in the flux range below 10^{18} Mx. The faculae are considerably smaller than their parent patches, and single magnetic patches contain single or multiple faculae. The faculae in general have higher intrinsic magnetic field strengths than the surrounding regions. We found that faculae flux alone cannot account for the magnetic flux from the polar region.

We investigated the role of photospheric flow fields in the formation and evolution of the polar magnetic patches. To obtain this we used a time series of maps of vector magnetic fields obtained with SP. We observed unipolar appearance and disappearance in the data. Converging horizontal flows are observed outside of the magnetic patches during the entire life time of the patches. The converging flow is best observed at a height close to the solar photosphere. We also observed a weak converging flow around the retraced patch location 16 minutes before the patch appearance. We suggest that polar magnetic patches are formed by the accumulation of flux fragments by the horizontal converging flows. In addition to direct cancellation between opposite polarity patches we observed unipolar disappearance of polar patches. We speculate that these patches diffuse away into smaller fragments with flux below the detection limit of the instrument and eventually undergo cancellation with opposite polarity fragments.

To understand the various mechanisms involved in the reversal of the polar magnetic field and the dynamic activities caused by the interaction between flows and magnetic field, continuous observations with high spatio-temporal resolution are necessary.

Contents

Chapter 1

Introduction

1.1 The Polar Magnetic Field

The diverse and dynamic phenomena occurring on the Sun is a consequence of interaction between solar plasma and the Sun′s magnetic field. The magnetic activity of the Sun is characterized by its cyclic variation with a period of 22 years. According to current understanding, the Sun′s magnetic field is produced and maintained by a solar dynamo (Babcock 1961; Leighton 1969; Charbonneau 2010). The Sun′s large-scale magnetic field is decomposed into toroidal and poloidal components. The dynamo mechanism involves recycling of these two components. The intense toroidal flux tubes, produced by the differential rotation acting upon the poloidal field emerge buoyantly through the solar convection zone and manifest on the surface as tilted bipolar sunspot pairs. The sunspots eventually decay and the remnant magnetic flux, dominant contribution to which comes from the trailing sunspots, is then transported to the polar region to regenerate the poloidal magnetic component (Babcock 1961; Leighton 1969).

The polar magnetic fields attain maximum strength during solar cycle minimum (corresponds to a period of minimum sunspot number) and become weak near the solar cycle maximum. One of the remarkable aspects of the polar magnetic field is its reversal around the maxima of 11-year sunspot cycles. Reversal of the polar magnetic fields was first reported by Babcock (1959). The 22-year magnetic cycle and the reversal of the polar magnetic field near the maximum of the solar cycle can be seen in Fig.1.1. Standard surface flux transport models interpret that the reversal of the polar magnetic fields is an outcome of magnetic flux transported to the polar caps from the active latitudes, by supergranular diffusion and meridional circulation (Babcock 1961; Leighton 1964; Wang et al. 1989; Sheeley 2005).

Reversal of the polar magnetic fields do not take place simultaneously in the north and south polar regions (Babcock 1959; Makarov & Sivaraman 1986; Shiota et al. 2012; Svalgaard & Kamide 2013). Rightmire-Upton et al. (2012) pointed out that the asymmetric polar field reversal may arise from the asymmetry in the meridional flow velocities. Some other studies suggest that the asymmetry in the polar field reversal is associated with asymmetric solar activity cycle in the respective hemispheres (Svalgaard & Kamide 2013; Mordvinov & Yazev 2014). The polar field reversal is reported to depend also on variation of the tilt angle of bipolar sunspots with latitude (Zolotova & Ponyavin 2013). They showed that an increase in the tilt angle of the spots with latitude is essential to reproduce the observed polar field reversal. The reversal is not an instantaneous process and in some solar cycles the polar region was observed to undergo two- or three-fold temporary reversals before the reversal is completed (e.g. Makarov & Sivaraman 1989; Benevolenskaya 1996).

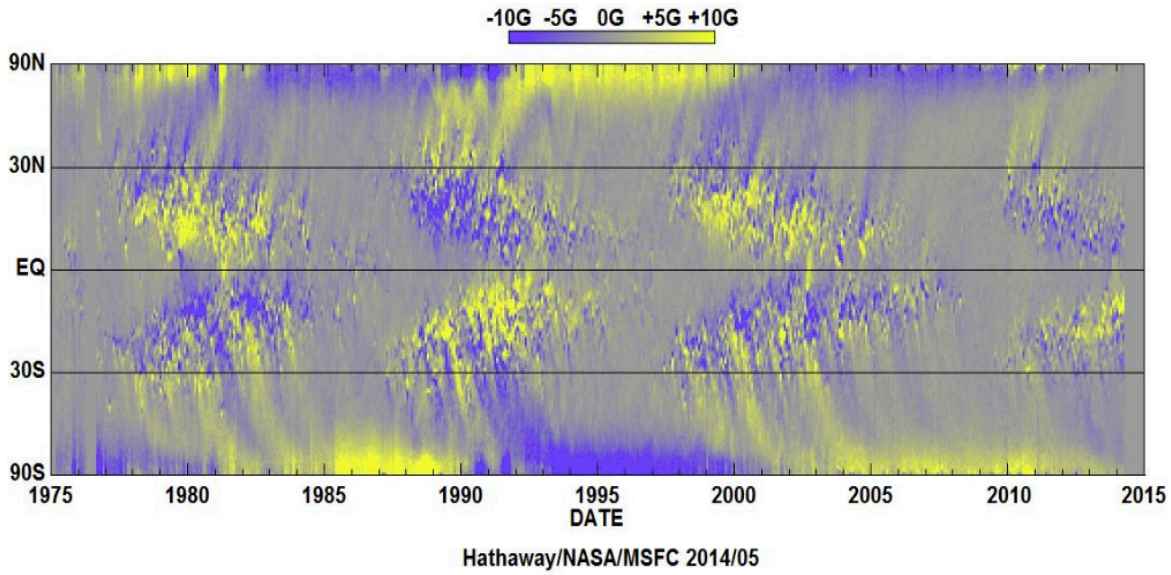

Figure 1.1: Magnetic butterfly diagram. The figure depict the radial component of the solar surface magnetic field. Reproduced from http://solarscience.msfc.nasa.gov/dynamo.shtml, which was prepared by D.Hathaway.

There are some distinct phenomena which mark the reversal of the polar magnetic fields. The rapid migration ("rush to the poles") of polar crown filaments (Hyder 1965, Makarov, Tlatov, & Sivaraman 2001), the disappearance of polar coronal holes (Waldmeier 1981, Harvey & Recely 2002) and cessation of high-latitude coronal mass ejections (CMEs)(Gopalswamy et al. 2003) indicate the onset of the polar field reversal. However, the mechanism that drives the polar field reversal is still an open issue and the prediction of the exact timing of the reversal is still difficult. Surface flux transport models suggest that the polar field reversal is realized by cancellation of the existing polar flux by the decayed active region flux of opposite polarity advected to the polar caps. Fisk & Schwadron (2001) argues that the reversal of polar magnetic fields is an outcome of the diffusive motions of the open magnetic field lines on the solar surface caused by their

reconnection with the randomly oriented closed loops. They also suggest that the reversal is a surface effect. Gopalswamy et al. (2003) proposed that the CMEs could be one of the possible mechanisms by which the open magnetic fields in the polar region decay during the reversal process.

The polar magnetic field and its reversal are of vital importance in understanding the origin of the solar magnetism and its periodic variation. Strength of the polar magnetic field in one solar cycle is employed to predict the strength of the successive solar cycle (Schatten et al. 1978; Choudhuri et al. 2007). The polar magnetic field is also considered as the origin of the fast polar solar wind. Despite the great importance of solar polar areas to understand numerous solar and astrophysical phenomena like the solar activity cycle, coronal heating, solar wind acceleration, etc., the polar regions are not yet sufficiently studied. The accurate measurement of polar magnetic fields is greatly limited by the foreshortening of the solar surface magnetic structures near the limb as well as instrumental limitations in terms of sensitivity and accuracy .

The previous studies on the polar magnetic fields were mainly based on line of sight (LOS) magnetograms. The observed magnetic fields are interpreted as the LOS component of the radial field and is corrected for by dividing by the cosine of the heliocentric angle (e.g., Svalgaard et al. 1978, Wang et al. 1989). Varsik et al. (1999) reported, using LOS magnetograms, that the polar caps are occupied by large unipolar regions which enclose magnetic knots of opposite polarities and that within a given unipolar region knots of one polarity dominate the other during cycle minimum. Using chromospheric LOS magnetograms Raouafi et al. (2007) speculated the possible existence of two kinds of magnetic concentrations in the polar regions: small flux elements which are uniformly distributed in the

polar caps, with a probable local origin and large flux elements originating from the decayed active region flux. The issues with the LOS magnetograms are; 1) the LOS component of the radial field does not produce large signals and hence the resulting field measurements will be weak, and 2) it is mixed with dynamic horizontal components (Harvey et al. 2007), which when corrected for projection effects might enhance noise signals.

To follow the distribution and cyclic variation of polar magnetic flux, proxies were and are still being used. Polar faculae, observed in the higher solar latitudes, are one such proxy. They are bright and are associated with magnetic fields. Polar faculae exhibit a periodic variation which is out of phase with the solar cycle (Saito & Tanaka 1960, Makarov & Makarova 1996, Deng et al. 2011). The cyclic variation of sunspot number and polar faculae count are shown in Fig.1.2. The count of polar faculae is considered as good proxy for the polar magnetic flux.

Faculae observed at lower heliographic latitudes near the limb are referred to as ″active region (AR) faculae″. They are seen particularly around sunspot active regions. Excess brightness of both AR and polar faculae in comparison with the quiet sun continuum intensity is explained based on the "hot wall effect" (Spruit 1976, Keller et al., 2004). Faculae are generally described as magnetic features with vertically oriented evacuated flux tubes. As a result of evacuation, flux tubes appear transparent. When observed at an inclined angle the hot wall of the flux tubes is visible causing the flux tubes to appear bright ("hot wall effect") in the continuum intensity images. Another important aspect that make the study of faculae, whether AR or polar, an interesting research topic is its contribution to the variations in total solar irradiance (e.g., Foukal et al. 2004).

The advantage with Hinode (Kosugi et al. 2007) is that it enabled unprece-

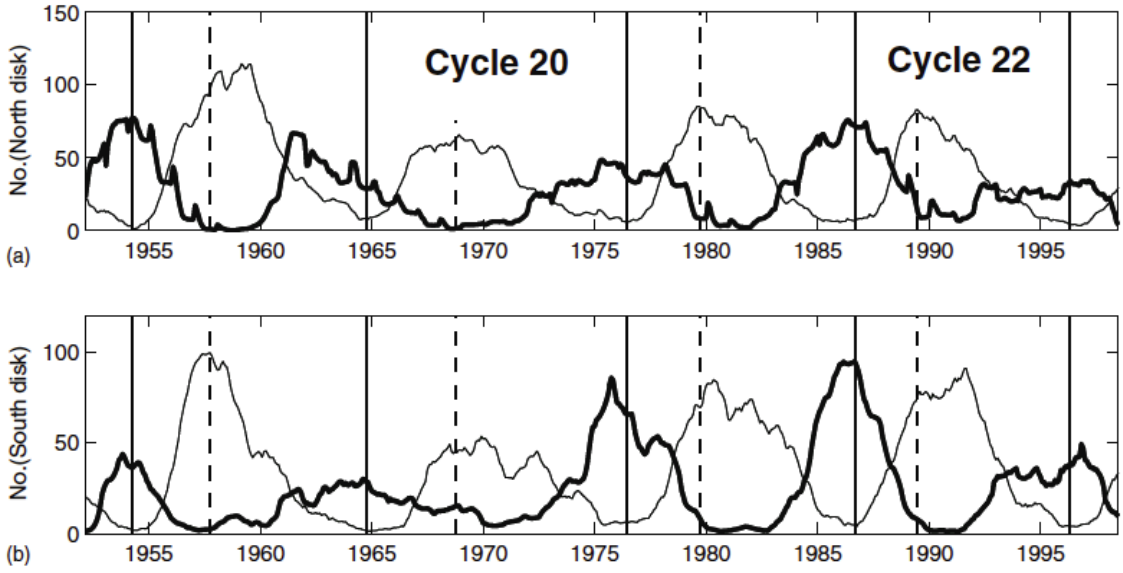

Figure 1.2: The smoothed monthly sunspot numbers (solid black line) and polar faculae (bold solid black line), in the northern hemisphere (a) and southern hemisphere (b), respectively. The vertical solid and dashed lines represent the minimum and maximum of each solar cycle, respectively (Deng et al. 2011). Polar faculae data were taken from National Astronomical Observatory of Japan (NAOJ) and sunspot data from Temmer et al. (2006).

dented observations of the polar regions with high spatial resolution and polarimetric (magnetic) sensitiveity and provides vector magnetic field information. Recent high-resolution observations with the spectropolarimeter (SP; Lites et al. 2013) of the Solar Optical Telescope (Ichimoto et al. 2008; Shimizu et al. 2008; Suematsu et al. 2008; Tsuneta et al. 2008b) aboard Hinode have shown that the polar region is dominated by unipolar magnetic patches of concentrated magnetic fields oriented vertical to the local surface with strengths exceeding 1kG (Tsuneta et al. 2008a; Ito et al. 2010). Tsuneta et al. (2008a) reported that the kilogauss patches exhibit spatial coincidence with polar faculae. Using observational data taken during the period of solar cycle minimum, Ito et al. (2010) found that the average area and the total magnetic flux of the polar patches are larger than those of the quiet Sun region in the lower latitudes. They also observed that the vertical flux distribution is balanced in the low-latitude quite Sun, whereas it is asymmetric in the polar region; The vertical flux distribution with the polarity same as that of the polar magnetic field dominates over the other polarity. They also found that total magnetic flux of the polar region is larger than that of the quiet Sun. Shiota et al. (2012) reported that the magnetic patches in the polar region are classified into two categories: the small-flux concentrations ($<10^{18}$ Mx), which are of mixed polarity with balanced fluxes, and the large-flux patches ($\geq 10^{18}$ Mx) scattered over the polar region, which are unipolar. The authors also found that large-flux patches are modulated by the solar cycle.

1.2 Purpose of the Thesis

The Sun's polar magnetic field plays an active role in manifesting many of the observed dynamic phenomena in the Sun. To throw light into these solar phenomena it is crucial to comprehend the evolution and properties of the polar magnetic fields in both global and local scale. Erstwhile studies focused mainly on the cyclic variation of polar magnetic flux rather than on their local scale distribution and evolution. As polar magnetic flux is concentrated in the form of patchy structures, it is the aggregate of this individual patches that contribute to the global scale behavior of the polar magnetic flux over the course of solar cycles. The main focus of this thesis is to understand the properties of individual polar magnetic patches and the role of photospheric plasma flows in the formation and evolution of such patches.

High resolution spectropolarimetric observations provided by Hinode has made the direct determination of magnetic flux of individual polar patches possible. However, the fine structure and properties of individual polar patches in terms of distribution of magnetic parameters and intensity are yet to be investigated. Further, the relation between polar magnetic patches and polar faculae, which are used as proxy while studying the cyclic variation of polar magnetic flux, is also unknown. Comprehension of this relationship is essential to understand the contribution of polar faculae to the polar flux. Though polar flux is believed to be originated from surplus magnetic flux of the decayed active regions, it still remains unexplored as to how: a) magnetic flux in the polar region is concentrated in the form of unipolar magnetic patches, and b) these magnetic patches decay and eventually reverse the polarity of the polar field.

Chapter 2 describes statistical study of: a) the association between polar magnetic patches and polar faculae, and b) the properties of the magnetic patches like magnetic field and its local zenith angle, intensity, etc using observations from Hinode SOT/SP of the north polar region. Chapter 3 mainly delineates the influence of photospheric surface flows in the evolution of polar magnetic patches. SP observations of the north and south polar region, with 16 min cadence and 6 hr duration, are used for this study. Finally, summary of the thesis is outlined in Chapter 4.

Chapter 2

Association between Polar Faculae and Polar Magnetic Patches

2.1 Introduction

Polar faculae are bright, small-scale structures visible in white light and in chromospheric lines. They populate higher heliographic latitudes, above 60° (e.g.,Okunev & Kneer 2004; Blanco Rodríguez et al. 2007) or 70° (Muñoz-Jaramillo et al. 2012). Okunev & Kneer (2004) found that the contrast of polar faculae decreases monotonically toward the extreme limb, whereas Blanco Rodríguez et al. (2007) reported that the contrast remains constant or may even increase toward the limb.

The number of polar faculae is considered to be a good proxy for the polar magnetic flux. It follows an 11 yr cycle that is out-of-phase with the sunspot

cycle (Makarov & Makarova 1996; Sheeley 2008; Muñoz-Jaramillo et al. 2012). The faculae become visible after the reversal of the polar magnetic field around sunspot maximum, and their numbers reach a maximum at sunspot minimum. Homann et al. (1997) and Okunev & Kneer (2004) found that polar faculae have magnetic field strengths in the kilogauss range and that they are unipolar, with the same polarity as the observed global polar field. However, Blanco Rodríguez et al. (2007) reported the existence of faculae having polarities opposite to that of the polar field.

Tsuneta et al. (2008a) reported that the kilogauss patches coincide in position with polar faculae, but the true nature of the relationship between polar faculae and the polar magnetic patches remains elusive. In this paper, we investigate how closely the faculae are associated with the magnetic patches by studying their polarity and intrinsic field strength, the inclination of the magnetic field vector with respect to the local normal (zenith angle), and their contribution to the magnetic flux of the observed polar region. We also attempt to determine parameters that control the brightness of polar faculae. These observations correspond to a phase of solar minimum and, hence, to a maximum of polar faculae. At the time of the observations, the polarity of the north polar cap was negative. We hereafter refer to magnetic patches with negative polarity as *majority* (dominant) polarity patches and those with positive polarity as *minority* polarity patches.

2.2 Observations

Information about the north polar region observations carried out by the Hinode SOT/SP in 2007 September is given in Table 2.1. Each map of the polar region

was acquired through several hours of slit-scan observations. The SP provides the full Stokes I, Q, U, and V profiles of the Fe I 630.15 and 630.25 nm spectral lines, including the nearby continuum with a spectral sampling of 2.155 pm. The integration time for each slit position is 9.6 s. The scanning step is $0''.15$ and the spatial sampling along the slit is $0''.16$. The raw SOT/SP data were calibrated using the *sp_prep* routine (Lites and Ichimoto 2013), available in the SSW package to account for dark current, flat fielding, instrumental cross talk and orbital drift along the wavelength axis. The noise level estimated from the continuum in the Stokes V spectrum is $1.1\times10^{-3}I_{\rm c}$, where $I_{\rm c}$ is the continuum intensity.

The magnetic field parameters are deduced by using a least-squares fit to the Stokes profiles using the MILOS code (**Mil**ne-Eddington Inversion of P**o**larized **S**pectra; Orozco Suárez & del Toro Iniesta 2007). MILOS assumes a two-component atmosphere model (magnetic and nonmagnetic) in a pixel. The inversion code provides: three components describing the vector magnetic field - the field strength B, the inclination between the line-of-sight (LOS) and the field vector, and the azimuth of the field vector in a plane perpendicularar to the LOS, the LOS velocity, two parameters describing the linear source function, the ratio of line to continuum absorption coefficients, the Doppler width, the damping parameter, and the stray-light factor α. The stray-light factor, α quantifies contribution to the measured intensity from both a non-magnetic area of the pixel and stray light contamination arising from instrument optics. From the stray-light factor the magnetic fill fraction - fraction of a pixel occupied by magnetic field - is calculated as $f = 1 - \alpha$(Orozco Suárez et al. 2007), provided the stray-light contamination is negligible. All these parameters are in the observer's frame.

The inversion is performed only for pixels whose linear or circular polarization

signal amplitudes exceed a given threshold above the noise level which depends on the exposure time. The noise level σ' is determined in the continuum wavelength range of the Stokes V profiles and is given by $\sqrt{\sum_i (V_i - \overline{V})^2/n)}$, where V_i is the intensity of the Stokes V profile at continuum wavelength pixel i, $\overline{V}$ is the average Stokes V signal for the same wavelength range, and n is the number of wavelength data points. The pixels with Stokes Q, U or V peak larger than 5 times the noise level alone are fitted using the code. Those pixels with the absolute value of the Doppler velocity higher than 10 km s^{-1} or the filling factor less than 0.01 are removed since it was found that the Stokes profiles of such pixels are not fitted well.

The azimuth value provided by the inversion is ambiguous by 180°. This ambiguity in the transverse magnetic fields was resolved by employing the method of Ito et al. (2010): The vector magnetic field for each pixel will have two solutions for the local zenith angle as a result of the ambiguity. We assume that the magnetic field vector is nearly vertical to the local solar surface and the ambiguity was resolved by selecting the value with the most vertical field in the local frame.The direction is deemed to be vertical if the zenith angle is between 0° and 40° or between 140° and 180°.

For this study we consider only the vertical magnetic field as the magnetic field vectors associated with polar patches are nearly vertical to the local surface (e.g., Tsuneta et al. 2008a).The vertical magnetic flux is defined as $\sum_j B_j f_j \cos i_j A_j$, where B_j, f_j, i_j, and A_j are the intrinsic field strength, magnetic filling factor, local zenith angle, and pixel area, respectively, for the jth CCD pixel. The pixel area was corrected for projection effect. Since the magnetic field in the polar region is distributed as isolated patches, neighboring pixels with the same polarity are

grouped into patches following the method described by Shiota et al. (2012), and each is given a signed identification number based on its polarity.

2.2.1 Identification of Polar Facular Pixels within Magnetic Patches

Magnetic patches at heliographic latitudes above 70° with at least 4 pixels, corresponding to the spatial resolution of the telescope, were selected for our study. Patches with μ (cosine of the heliocentric angle) less than 0.126, corresponding to a heliocentric angle of 82°.8, were ignored, since the granular structure is not recoverable beyond this angle.

We picked up magnetic patches and then identified facular pixels inside each patch in the normalized continuum intensity maps. The continuum intensity (I_c) map is obtained by integrating the Stokes I profile outside the absorption lines. The integration ranges were 6300.98–6301.08 and 6302.90–6302.99 Å. A smoothed map representing the center-to-limb variation (CLV) of the continuum intensity, $\langle I_c \rangle$, is obtained as follows: A least-squares surface fit using a 5th-order polynomial in μ (following Pierce et al. 1977) is performed on the I_c map. The fitted map is then subtracted from the original, and the standard deviation σ_0 of the difference is calculated. We then remove the bright and dark features from the original image using a $\pm 3\sigma_0$ cutoff, and a fit with same functional form is performed to obtain a CLV function unaffected by the presence of faculae. The normalized intensity is defined as $I_c/\langle I_c \rangle$, where I_c and $\langle I_c \rangle$ are the continuum intensity and the intensity averaged over the same μ-value, respectively. An example of continuum intensity map and the corresponding normalized intensity map are shown in Figures 2.1 and

2.2 respectively.

Figure 2.3 shows the scatter plot of normalized intensity as a function of μ. The spikes in the plot are attributed to polar faculae, while smaller fluctuations about 1.0 are ascribed to granulation. Within each magnetic patch, pixels having intensity greater than or equal to a given threshold are classified as belonging to polar faculae. The threshold to identify facular pixels varies with μ. The standard deviation σ of the normalized intensity (with respect to the smooth CLV function) is derived at each μ with a bin size of 0.01, and the σ's are fitted with a 3rd-order polynomial in μ for each of the six observations. The threshold to detect faculae is set to 4 σ, which is well above the intensity fluctuations due to granulation, as shown in Figure 2.3 (thick solid line).

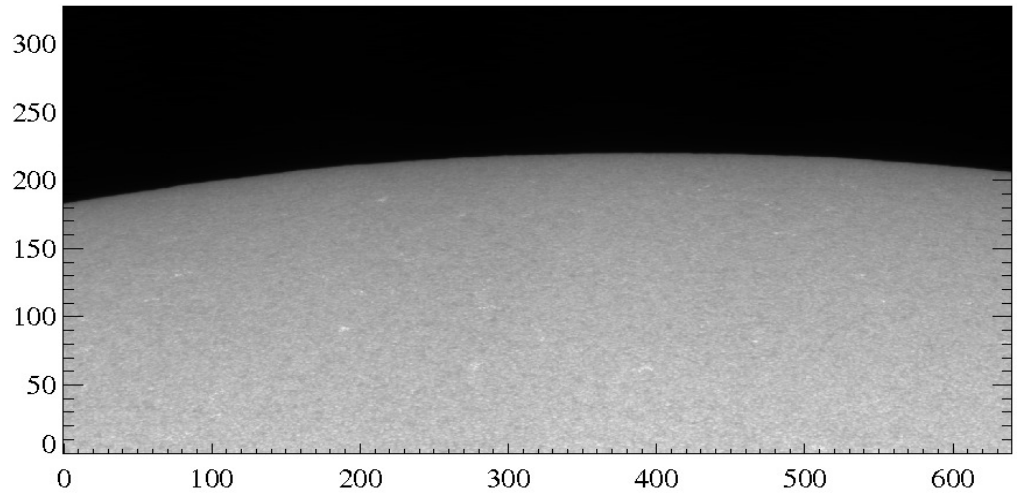

Figure 2.1: The continuum intensity map (2007 September 6). The x and y axes are in arcsec.

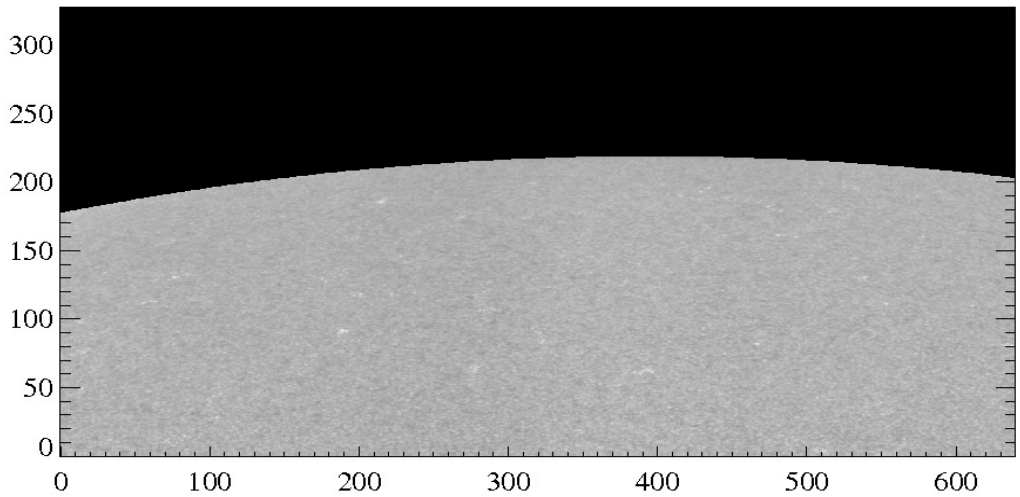

Figure 2.2: The normalized intensity map (corresponding to Figure 2.1) corrected for limb darkening (2007 September 6). The x and y axes are in arcsec.

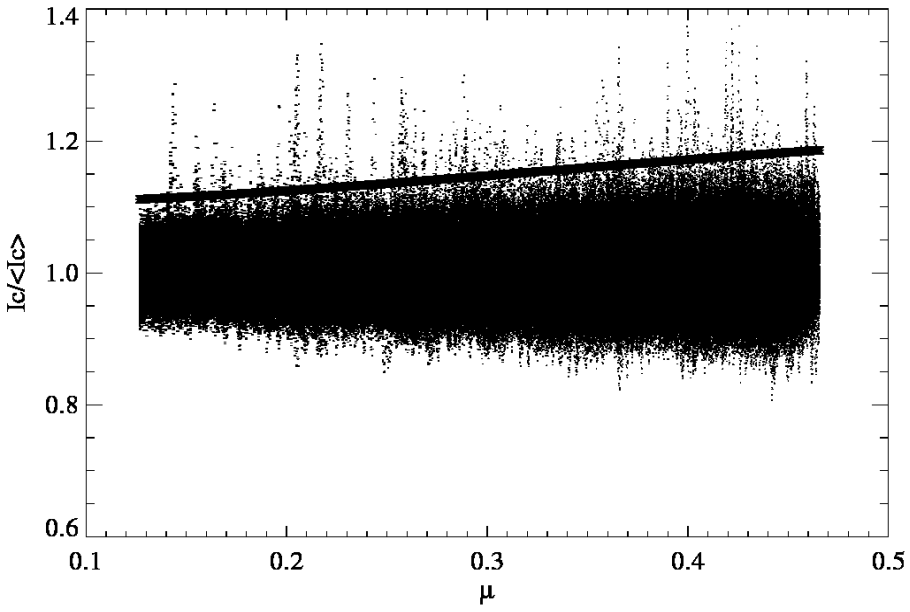

Figure 2.3: Normalized continuum intensity vs. μ for all pixels (2007 September 4). The μ-values increase with distance from the limb. In this plot, the polar faculae appear as intensity spikes. Both granular and facular intensities decrease toward the limb. The thick solid line indicates the 4 σ fluctuation threshold used to pick out faculae. The value 1.0 is the quiet-Sun intensity averaged over same μ-value.

Table 2.1: *Hinode* Data Set

Date	Time (UT)	Exp. time (S)	Field of View[a]				TMF[b] $\times 10^{20}$ Mx	PFF/TMF[c] (%)	MPF[d] $\times 10^{19}$ Mx
			Xmin (arcsec)	Xmax (arcsec)	Ymin (arcsec)	Ymax (arcsec)			
2007 Sep 04	18:13-23:42	9.6	-194.86	125.12	841.81	1005.65	9.06	16.74	3.01
2007 Sep 06	00:28-05:57	9.6	-197.28	122.72	842.43	1006.27	12.4	18.2	3.71
2007 Sep 08	01:07-06:36	9.6	-186.08	133.92	840.67	1004.51	13.15	15.2	2.67
2007 Sep 09	01:05-06:35	9.6	-186.72	133.28	842.35	1006.19	10.0	11.26	2.68
2007 Sep 10	01:15-06:39	9.6	-200.00	115.00	841.47	1005.31	12.3	16.5	2.10
2007 Sep 16	01:23-06:52	9.6	-183.52	136.42	832.25	996.09	10.56	15.0	3.75

[a]In heliographic coordinates. X is directed toward solar west and Y toward solar north. The origin of the coordinate system is Sun center.
[b]Total vertical magnetic flux contributed by all the majority polarity patches (with flux $\geq 10^{18}$ Mx), both with and without polar faculae.
[c]PFF denotes the total magnetic flux from polar faculae associated with majority polarity patches with flux $\geq 10^{18}$ Mx detected in this study.
[d]Total magnetic flux contributed by all the minority polarity patches (with flux $\geq 10^{18}$ Mx), both with and without polar faculae.

2.3 Results

We find that polar faculae, as defined above, are present in about 55% of the majority polarity magnetic patches with flux greater than 10^{18} Mx (Figure 2.4). Concentrations of large magnetic flux, which vary with the solar cycle (Shiota et al. 2012), harbor polar faculae. Numerous patches without faculae also exist in the polar region; at fluxes below 10^{18} Mx, patches without faculae far exceed those with faculae.

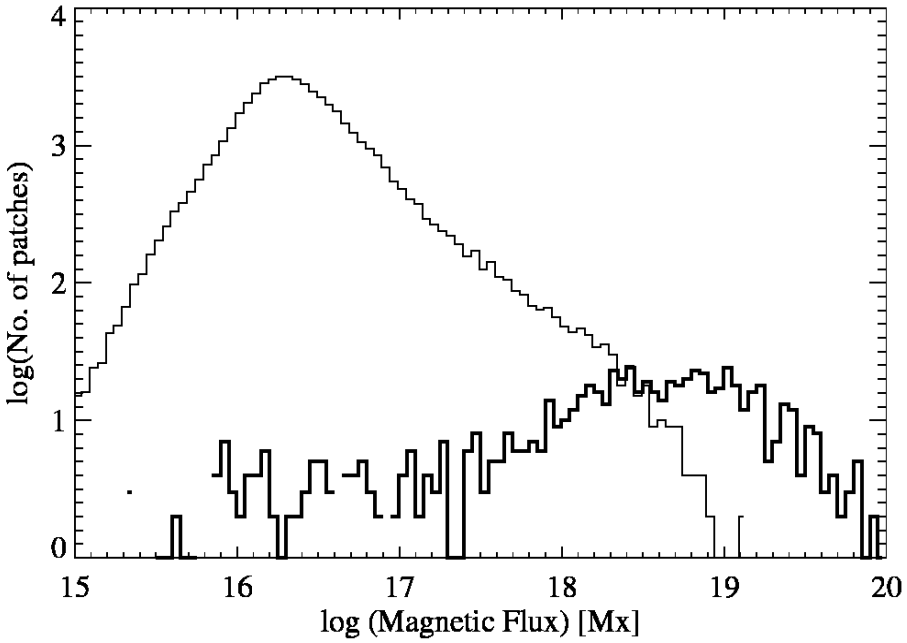

Figure 2.4: Histogram of the magnetic flux of the majority polarity patches. The thick line represents patches that contain one or more faculae, and the thin line shows patches without faculae. The values shown on the x-axis correspond to flux per patch. The magnetic flux of a patch was obtained by integrating the flux of all pixels within the patch.

2.3.1 Majority Polarity Patches

Here we focus on majority polarity magnetic patches with polar faculae. We find that the patches with faculae are not uniformly bright but instead contain smaller faculae. Figure 2.5 shows two examples of patches with polar faculae. In the first (panel (a)), four faculae are identified in one patch. They differ in size, intensity, and magnetic flux. In most cases, the facular islands enclose the local flux maximum within the magnetic patch (e.g., the two uppermost faculae in panel (b)). In the second patch (panel (c)), only one facula is identified. These examples reflect the general case that the number of polar faculae associated with each patch ranges from one to a few. The faculae have fine structure, with a core and an extended halo region (represented by arrows A and B, respectively, in Figure 2.5).

Each magnetic patch is taken to comprise two components: a polar facular region and a nonfacular region. As polar faculae are small structures compared with the nonfacular region within a patch, it is reasonable to use the peak value of $I_c/\langle I_c \rangle$ rather than its average value to characterize the faculae, to better capture localized behavior. We refrain from plotting the peak values against flux for nonfacular regions, as it is possible that our threshold might misclassify some true facular pixels as nonfacular. Such errors, if any, could be minimized by taking the average of the normalized continuum intensity. The top panel of Figure 2.6 is a scatter plot of the peak intensity inside the polar faculae versus their magnetic flux. For each patch, the peak intensity was obtained by considering all the facular pixels in the patch, and the magnetic flux was calculated by summing the flux of all the facular pixels within the patch. There is a clear positive correlation

between the peak intensity and the magnetic flux. For magnetic fluxes $\leq 10^{17}$ Mx, the peak intensity lies between 10% and 20% above the average, beyond which it increases from 20% to 44%. This trend can be explained with the results from Venkatakrishnan (1986), who discovered that convective instability is less efficient for flux tubes with lower magnetic flux ($\leq 10^{17}$ Mx). This is a consequence of efficient thermal coupling between smaller flux tubes and the ambient nonmagnetic atmosphere, which hinders convective collapse. Observational confirmation of this finding was given by Solanki et al. (1996) using quiet-Sun data near disk center. Hence, the faculae need to have minimal magnetic flux to be visible as distinct magnetic features.

In the bottom panel of Figure 2.6, we map the normalized intensity averaged over facular (crosses) and nonfacular (triangles) regions against their respective fluxes. The average intensity of the faculae increases with magnetic flux, as expected. A comparison of the two panels makes clear that for faculae, peak intensity is better correlated than average intensity with the magnetic flux. The bottom panel also shows that the average intensity of nonfacular regions decreases with magnetic flux. This bimodal distribution is essentially the same for different μ-ranges. For a given flux value, there exist both bright facular and darker nonfacular regions. Hence, magnetic flux cannot be used to discriminate between facular and nonfacular regions within a magnetic patch. Note that the branching becomes evident at fluxes greater than 10^{17} Mx. The magnetic patch with large magnetic flux is larger in size and hence it is likely that the nonfacular region in such magnetic patch will mostly be occupied by granules . We think this is the reason why the average intensity of the nonfacular region approaches unity with increasing magnetic flux.

In Figure 2.7, we plot the probability distribution functions (PDFs) of intrinsic field strength averaged over facular and nonfacular pixels within each magnetic patch. The average field strength of the polar faculae displays a broad peak at 700–1000 G. The nonfacular regions exhibit a peak around 400 G. Since the degree of the depression of the visible surface in a flux tube depends on the intrinsic magnetic field strength, this sharp difference is consistent with the picture set forth by Spruit (1976; see Section 4).

Figure 2.7 also shows, however, that some faculae have very small average intrinsic magnetic field strengths. The field strength may decrease toward the limb as a result of our viewing greater heights in the atmosphere, thus leading to weaker observed fields. In this case, the low values of magnetic field strength would correspond to those from smaller μ. Our examination did not identify any trend in this relationship. We also found that the average intensity of these faculae does not show any dependence on the intrinsic field strength averaged over the respective facular pixels. It is not clear whether these represent different evolutionary phases of faculae, and so to clarify the situation, it will be necessary to examine the temporal evolution of the magnetic patches.

The PDFs of the zenith angles of the magnetic field vectors averaged over facular and nonfacular pixels within each magnetic patch are shown in Figure 2.8. The vectors of both regions are nearly vertical to the local normal, but those of nonfacular regions appear to be slightly inclined. The PDF of the zenith angle has a peak at approximately 169° for facular regions and a maximum around 165° for nonfacular regions. This small but clear difference may reflect a tendency of faculae to be located in a less diverging portion of the fanning-out field lines (Tsuneta et al. 2008a) of magnetic patches.

The PDF of the average filling factor for polar faculae shows a broad distribution ranging from 0.1 to 0.6 (Figure 2.9), while the nonfacular regions have a distinct peak at ∼0.2. Although some polar faculae have a very high filling factor, there exists no significant difference between facular and nonfacular regions within magnetic patches as compared with the intrinsic field strength or the zenith angle of the magnetic field vector, as is evident from Figures 2.7 and 2.8. Figure 2.10 depicts the variation with μ of the average intensity of polar facular regions within each magnetic patch. The intensity decreases gradually toward the limb, consistent with Okunev & Kneer (2004).

2.3.2 Minority Polarity Patches

We find that polar faculae are associated with minority polarity patches as well, which is to say, they are polarity independent. However, faculae with minority polarity are very limited in number, and most have magnetic fluxes below 10^{18} Mx. Figure 2.11 is a scatter plot of the peak intensity of minority polarity faculae as a function of their magnetic flux. This should be compared with Figure 2.6 (top panel), for the majority patches. Peak intensity appears to have a positive correlation with magnetic flux. This indicates that irrespective of polarity both minority and majority polarity faculae exhibit similar behavior.

2.4 Discussion

We have found that polar magnetic patches have substructure, with one or more small faculae embedded in the much larger patches. The faculae appear to be a subregion of magnetic patches. Their shapes inside the patches are irregular. Most

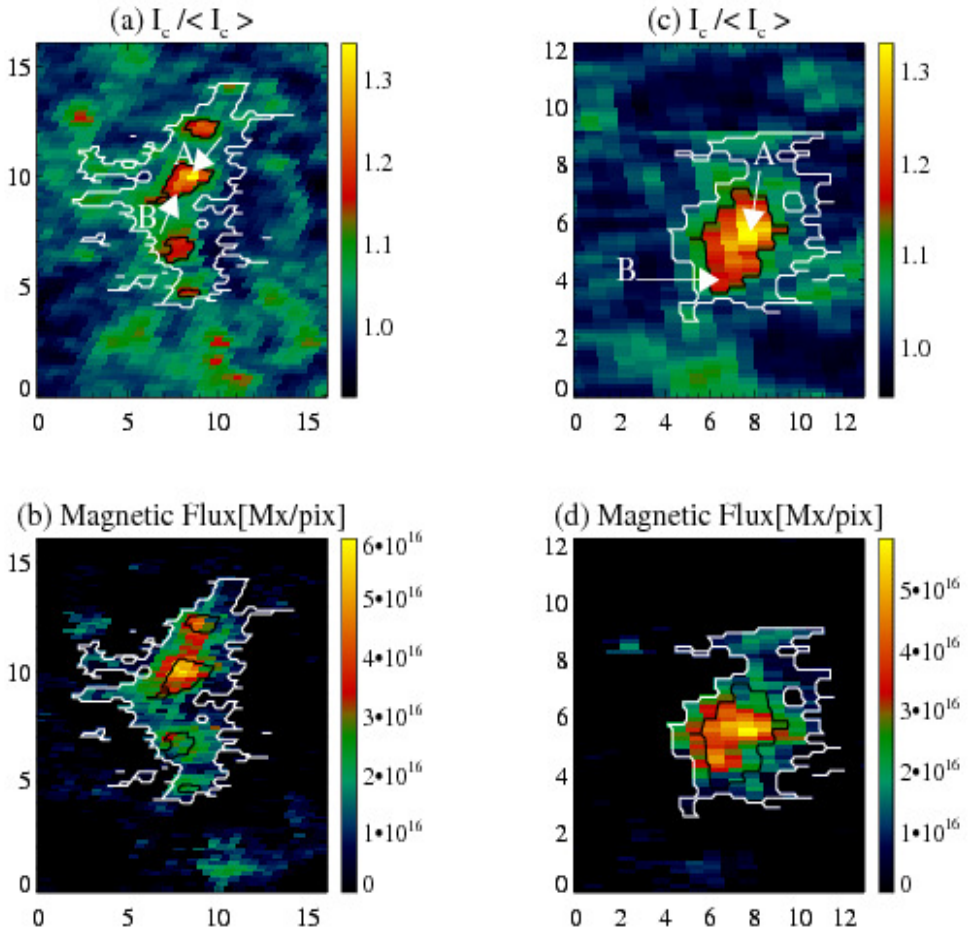

Figure 2.5: Two examples of magnetic patches associated with polar faculae: (a, c) normalized continuum intensity; (b, d) magnetic flux in units of maxwell per pixel. White contours enclose the patches, and black contours enclose the polar faculae within the patch. The x and y axes are in arcseconds. For patch 1 (left), the magnetic flux is 3.07×10^{19} Mx, and $\mu \approx 0.26$; for patch 2 (right), the flux is 2.24×10^{19} Mx, and $\mu \approx 0.21$. Arrows indicate core (A) and extended (B) regions of the faculae.

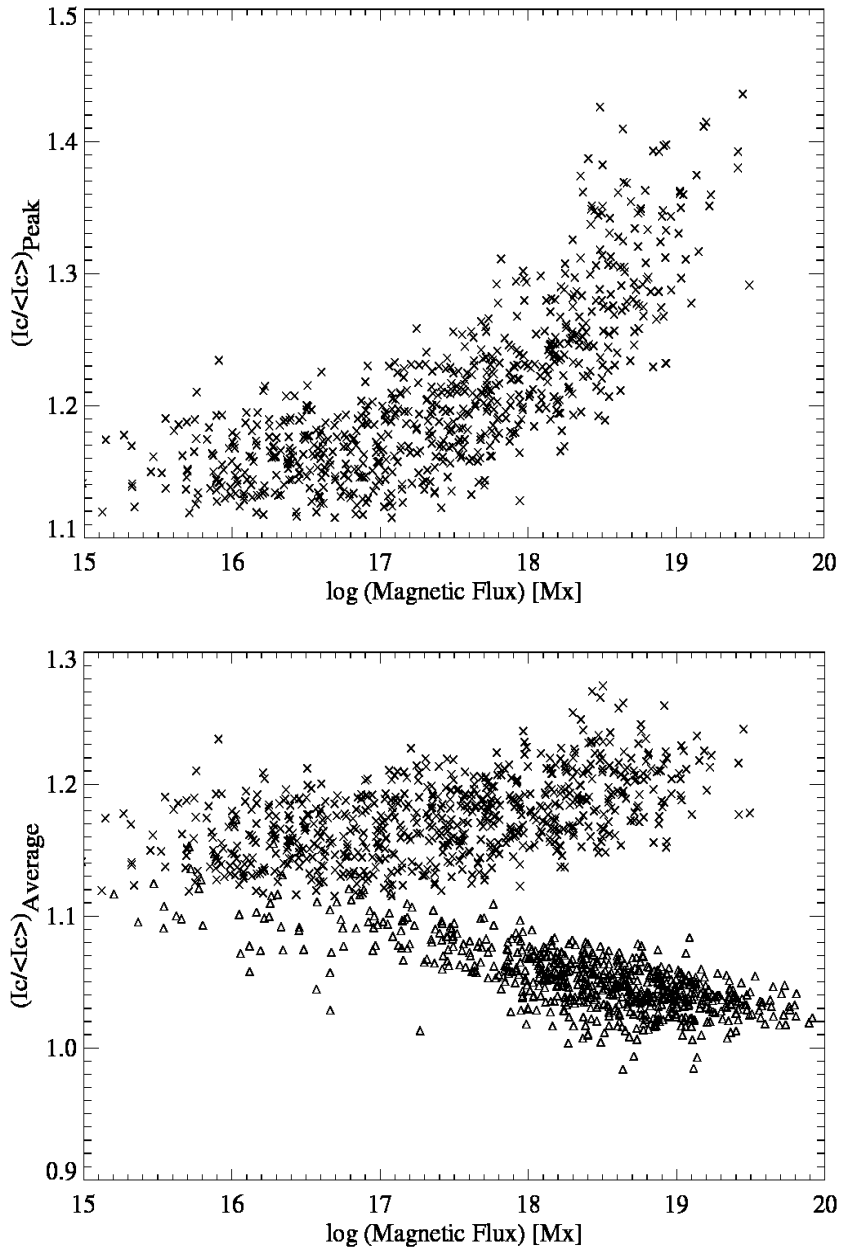

Figure 2.6: Top: Peak value of the normalized continuum intensity $I_c/\langle I_c\rangle$ of majority polarity polar faculae vs. magnetic flux summed over facular pixels within each magnetic patch. Bottom: Scatter plot of the average value of $I_c/\langle I_c\rangle$ of majority facular (crosses) and nonfacular (triangles) regions as a function of magnetic flux integrated over the respective pixels within each patch. Peak and average intensities of polar faculae are calculated over all the facular pixels identified within each patch. For each patch, the average intensity of the nonfacular region is determined by taking the mean of intensity of all the pixels outside faculae within that patch.

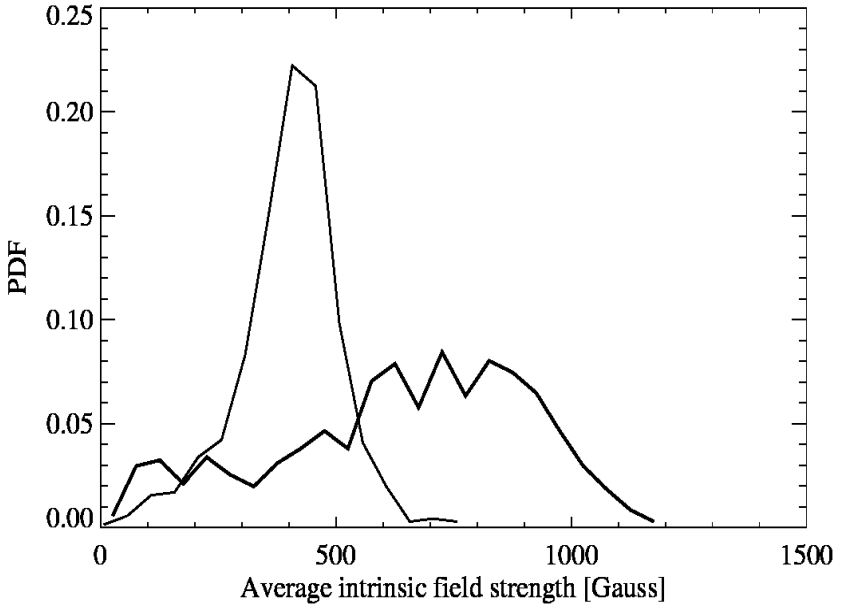

Figure 2.7: PDFs of average intrinsic field strength of polar facular (thick solid line) and nonfacular (thin solid line) regions within magnetic patches. The bin size is 50 G.

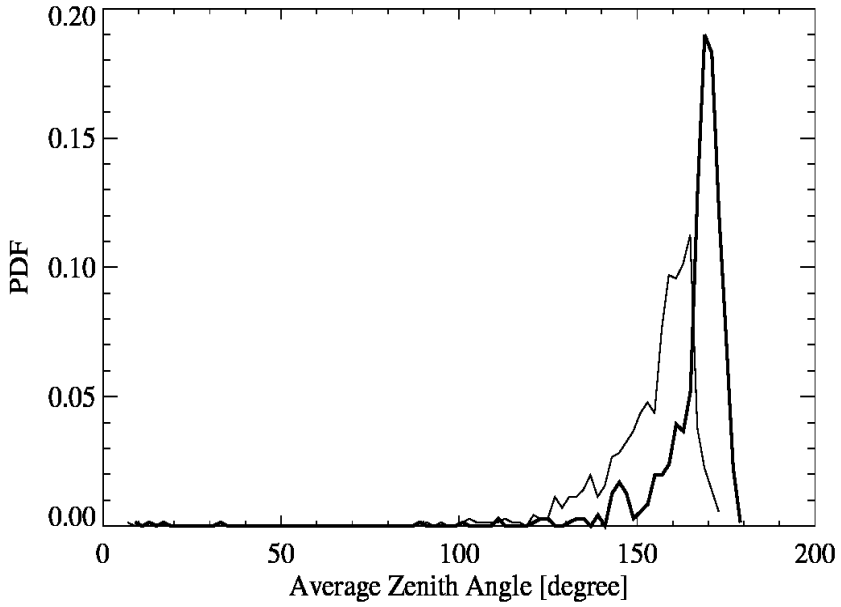

Figure 2.8: Same as Figure 2.7, but for average zenith angle. The bin size is 2°.

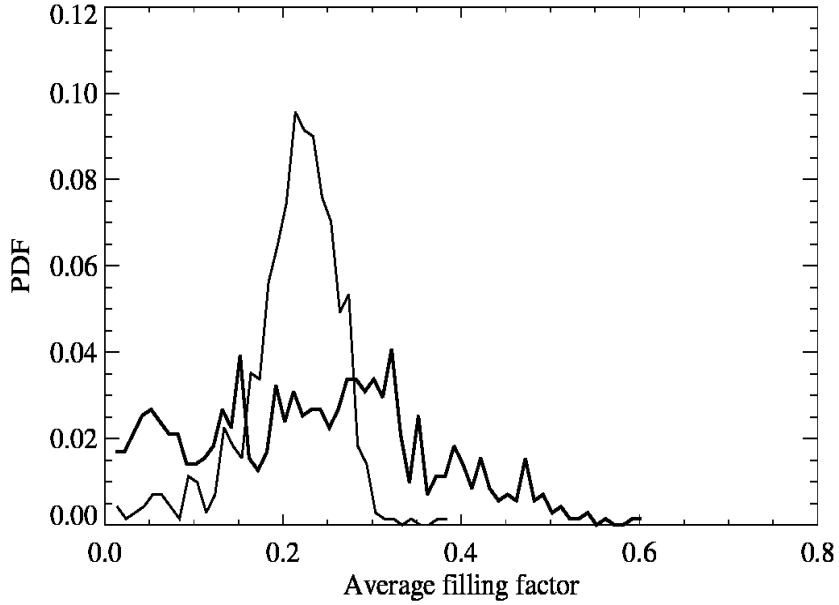

Figure 2.9: Same as Figure 2.7, but for average filling factor (see Section 2) The bin size is 0.01.

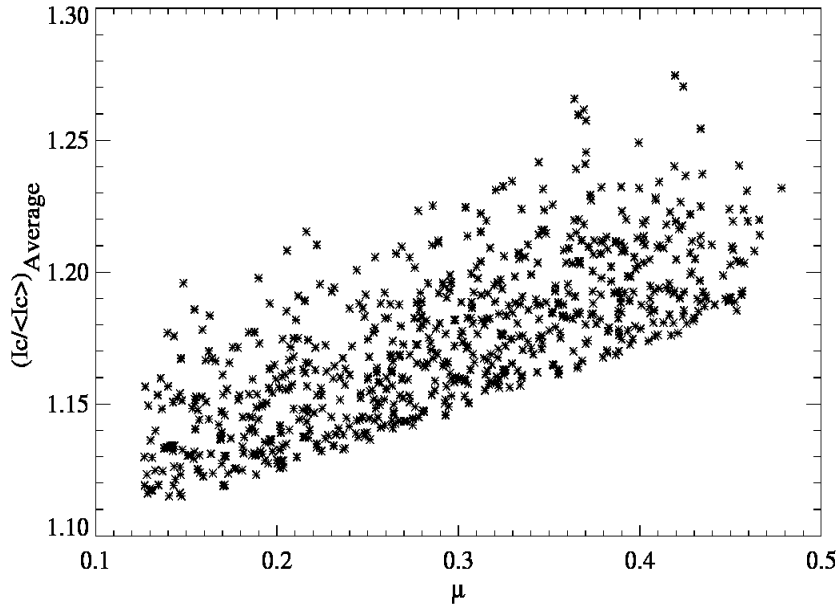

Figure 2.10: Scatter plot of the average normalized continuum intensity of polar faculae as a function of μ. The lower boundary of the distribution is due to the 4 σ threshold.

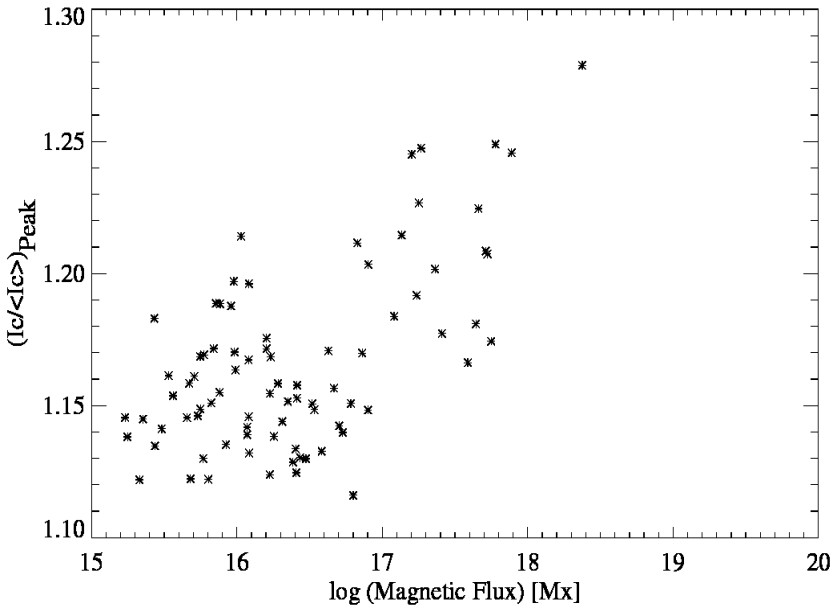

Figure 2.11: Same as the top panel of Figure 2.6, but for minority polarity faculae.

of the large magnetic concentrations, which have cyclic behavior, host faculae. We also found that faculae exhibit a tendency to have higher intrinsic magnetic field strengths compared with the nonfacular regions inside the associated magnetic patches. Table 2.1 lists the ratio of the magnetic flux of the faculae to that of the patches (including those without polar faculae). We find that less than 20% of the total magnetic flux from the large concentrations is accounted for by the associated faculae. It is important to study the cyclic variation of the facular flux contribution to the large concentrations in order to understand the exact relationship between polar faculae and the solar cycle.

We found that minority polarity faculae also exist in the polar region. The number of minority polarity faculae might depend on the strength of the unipolar field in the polar region. Hence, for weak solar cycles, care should be exercised in assuming that the count of polar faculae (which have been presumed to be unipolar

in most previous studies) is linearly related to the total signed polar magnetic flux.

We expected in this investigation to find controlling parameters and/or environment that switch polar faculae on or off. Intrinsic magnetic field strength and magnetic flux indeed correlate well with the existence of polar faculae, as shown in Section 2.1, but the correlation is somewhat ambiguous, as shown respectively in Figures 2.7 and 2.4. Polar faculae possess stronger and more vertical fields than their surroundings within a magnetic patch. This tendency may be due to the polar faculae being located near the patch centers.

Our observation that faculae possess strong vertical magnetic fields with average intensity decreasing toward the limb is consistent with the hot-wall model (Spruit 1976), which attributes the enhanced brightness of faculae to a depression in the visible surface caused by magnetic pressure, allowing an enhanced view of the hot wall of the flux tube at oblique angles.

We do not have information on the evolution of polar faculae during the development of the parent magnetic patches from just the snapshot slit-scan observations. It remains necessary to investigate the temporal evolution of magnetic patches and polar faculae to further constrain the properties of faculae.

Chapter 3

Photospheric Flow Field Related to the Evolution of Polar Magnetic Patches

3.1 Introduction

The Sun's polar caps are dominated by unipolar magnetic patches which possess magnetic fields in kilogauss range. According to current understanding, origin of magnetic flux in the polar region is the surplus flux from the decayed active regions transported to the polar cap via diffusion and meridional flow. Precisely how these incoming flux fragments are concentrated into patches or how they decay are not yet studied.

Transportation and concentration of magnetic flux by converging horizontal flows leading to the formation of magnetic structures are observed in the lower heliographic latitudes. Many of the dynamic phenomena observed on the Sun are

also the result of interaction of magnetic field with plasma flows. Most of the magnetic flux outside sunspots is concentrated and organized into a variety of multi-scale magnetic features by convective flows in the solar surface layers. The horizontal converging flows concentrate vertical magnetic flux predominantly at the convective cell boundaries. The magnetic flux is advected to the cell boundaries until the field strength reach the equipartition value which corresponds to the balance between magnetic pressure and dynamic pressure of the convective flows. Further intensification of magnetic fields to kG strengths is induced by the mechanism of convective collapse (Parker 1978; Spruit 1979).

Magnetic fields and photospheric plasma motions are well coupled and hence it is important to understand whether the flow field play any role in the formation and evolution of the polar magnetic patches. This information might give some insight to understand the mechanism involved in polar field reversal and the dynamical processes that could influence the overlying atmospheric layers. In this chapter we investigate the role of photospheric flow fields in the formation and evolution of polar magnetic patches. We also attempt to obtain precursor to the facula appearance within the patch. We used high spatio-temporal resolution observations obtained with the Spectropolarimeter(SP) of SOT/Hinode for this study. Section 3.2 describes our observation and analysis.The main results obtained are detailed in section 3.3 and summary and discussion on the results are given in section 3.4.

3.2 Observations

The data sets used in this study are given in Table 3.1. These data were taken from the north and south polar caps of the Sun with spectropolarimeter (SP) of the SOT aboard Hinode. The SP recorded full Stokes spectra of the two Fe I lines at 630.15 nm and 630.25 nm with the fast map mode whose slit-scanning step is 0.32″ and integration time in each step is 3.2s. The slit was along N - S direction. The spatial sampling along the slit is 0.32″ and the spectral sampling is 2.15 pm. Image sequences were obtained with a cadence of 16 minutes and the FOV was 80″ x 164″. The observations were taken in such a way that the solar limb and the pole is always within the FOV (e.g., left panel of Figure 3.2). The noise level σ is estimated from the continuum in the Stokes V spectrum and is 1.3 x $10^{-3} I_c$, where I_c is the continuum intensity. The inversion was performed only for those pixels with Stokes Q, U or V peak is larger than 5σ. Consecutive SP image frames are then aligned using spatial cross-correlation of the Stokes V maps, with pixel accuracy to compensate for the the image motion induced by the correlation tracker device on board the satellite. The spatial offsets thus obtained were used to register other relevant parameters.

To determine the solar limb position, a filtergram (NFI/SOT) image taken at time close to the time of scanning of the center of FOV of the first frame of the SP observations was used. The FG data (shuttered Stokes I and V) were taken at 140 mÅ red-ward of the Na I D_1 5896Å line center with a FOV of 327.7 ″x 163.8″(see Figure 3.1). The pixel size was 0″.16 and the the exposure time was 0.205 s. The fg_prep.pro procedure in the SolarSoftWare (SSW) package was used to subtract the bias and dark current of FG data. The solar limb position was then estimated

using the FG Stokes I image and was then fitted with a circle to calculate the pole positions. We used the large FOV FG image to obtain solar limb as it is required to minimize the error while fitting the limb with a circle to determine the pole position. FG and SP Stokes V (first scan of the observation) maps were then aligned using spatial cross-correlation to get the information on the limb and pole positions in the SP image scale (see Figure 3.2). This information is used to derive μ (cosine of the heliocentric angle) which is used to obtain the normalized intensity ($I_c/\langle I_c\rangle$).

Table 3.1: SP Observations

Date	Time (UT)	Center of FOV of the First Scan	Number of Frames	Number of Patches Selected
2013 Nov 11	10:22-16:43	(-15.0″, 917.4″)	24	12
2013 Nov 13	09:57-15:51	(-14.9″, -942.6″)	24	5
2013 Dec 08	09:00-15:47	(-14.8″, 917.3″)	24	10
2013 Dec 11	09:06-15:53	(-15.0″, -942.5″)	24	15
2014 Jan 17	09:06-15:53	(-14.9″, 917.3″)	24	13
2014 Jan 23	03:05-09:18	(-14.9″, -958.0″)	23	13
2014 Mar 08	11:06-17:43	(-14.9″, -957.8″)	24	7

The vector magnetic field and normalized intensity ($I_c/\langle I_c\rangle$) for the SP image sequences were obtained as described in section 2.2. The difference, in the calculation of $I_c/\langle I_c\rangle$, from the study in Chapter 2 is that the pixels in the magnetic patches are identified as facular pixels when their normalized intensity is greater than 3σ instead of 4σ. We found, by inspecting the variation of normalized intensity with μ that an intensity threshold of 3σ fits best for our current data set. The continuum intensity averaged over the same μ value is denoted by $\langle I_c\rangle$ and σ

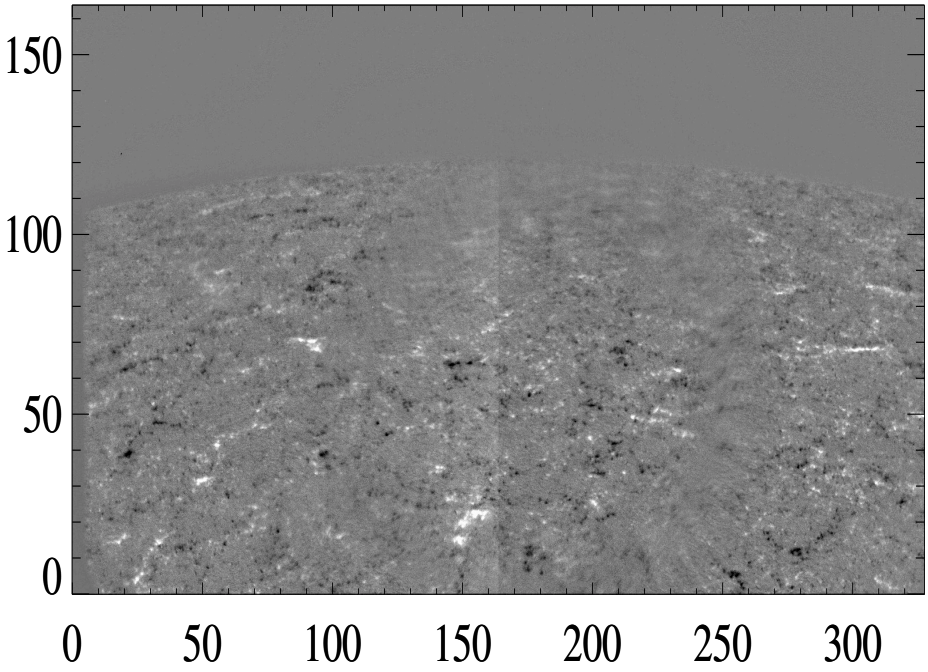

Figure 3.1: A sample FG Stokes V image (2013 November 11) with full FOV. The x and y axes are in arcsec. Center of FOV: (14.98″, 910.1″)

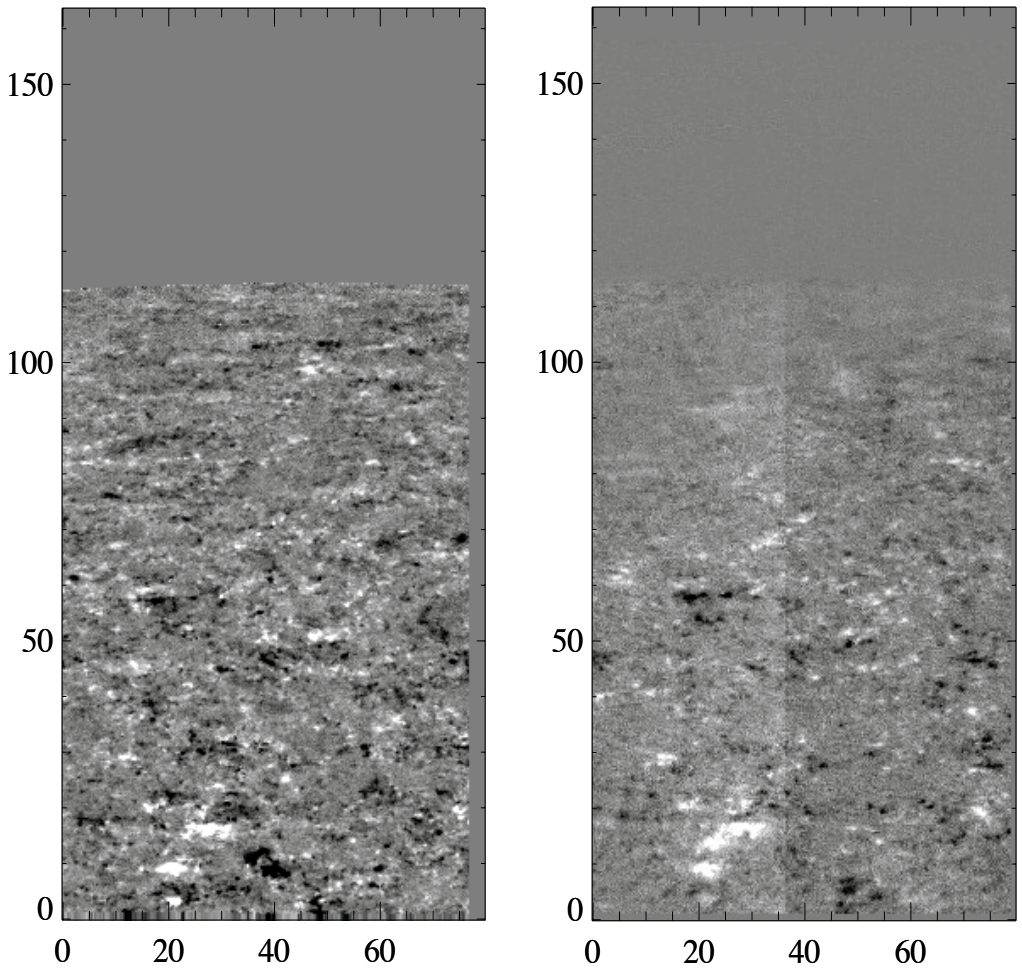

Figure 3.2: Left: Stokes V map of SP (2013 November 11). Right: FG Stokes V image (Figure 3.1) after alignment with the SP map on the left.The x and y axes are in arcsec.

is the standard deviation of $I_c/\langle I_c \rangle$.

3.2.1 Identification and Tracking of Magnetic Patches

The code developed by Iida (2012), which was used to identify and track network magnetic patches, in quiet Sun near disk center (for details see Iida 2012, Section 2.2.2) is employed here to select and track the polar magnetic patches. The modifications from Iida′s code and conditions used are detailed as follows. Magnetic patches must:

(1) be within the heliocentric latitude band of 70° - 80°

(2) have minimum size of 5 contiguous pixels

(3) have per pixel flux greater than 2 x 10^{16} Mx (1 sigma value obtained from the magnetic flux distribution)

We identify patches from the magnetic flux map with a clumping method. The clumping method chooses and groups all connected pixels which satisfy the above criteria into a single magnetic patch.

Here we consider a peak granular advective velocity of 1km/s (e.g., Berger et al. 1998) and that the lateral shift due to rotation ($\propto \sin\phi$, where ϕ is the colaitude) is small within the latitude range of 70° - 80° (see, Benevolenskaya 2007). So the magnetic patches are assumed to undergo a maximum displacement of about 4 pixel size within an interval of 16 minutes (1 km/s x 960 s = 960 km $\sim$ 4 pixels). The magnetic patches which spatially overlap in consecutive SP frames are marked as identical. The following patches have been eliminated from our samples: (a) patches which were present during the entire observation period, (b) patches which were present at the beginning of the observation, (c) patches which appeared in

the final frame, and (d) patches that are located at a distance shorter than 4Mm from the edge of the FOV. Those samples which were born and disappeared during the period of observation, with minimum life time of 3 frames are chosen. Finally, 75 magnetic patches in total satisfied all the above criteria.

3.3 Results

3.3.1 Lifetime and Magnetic Flux Distribution of the Samples

Here, we outline the general properties like lifetime and magnetic flux distribution of the 75 magnetic patches chosen as described in Section 3.2.1. The distribution of apparent life-time of the sample magnetic patches is shown in Figure 3.3. Most of the samples have a life time of 32 min (3 frames) and the average life time is about 1 h. Figure 3.4 shows the distribution of time-averaged magnetic flux of the patches. The average magnetic flux is $\sim 10^{18}$ Mx. This value is close to the lower limit of the large flux concentration mentioned in Shiota et al. (2012). Majority of the patches have positive polarity since patches with positive polarity are dominant in both the north and the south polar caps during our observation period. The patches with negative polarity (22 patches) come from both north and south polar region. There are many magnetic patches with larger flux which were present during the entire observation period (6 h) and are not considered in this study.

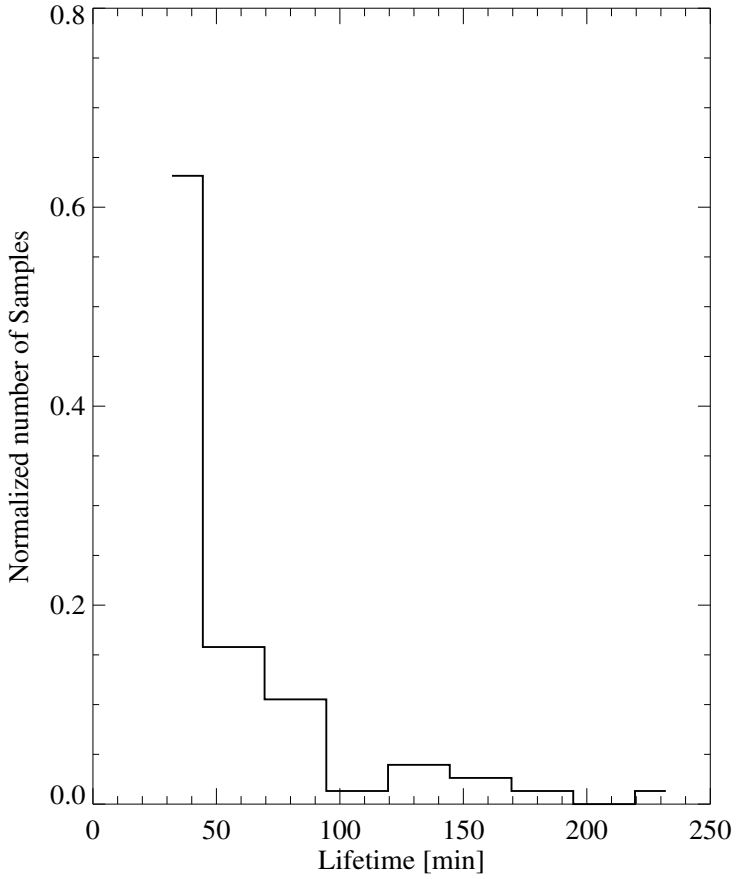

Figure 3.3: Distribution of lifetime for the 75 sample patches selected for this study.

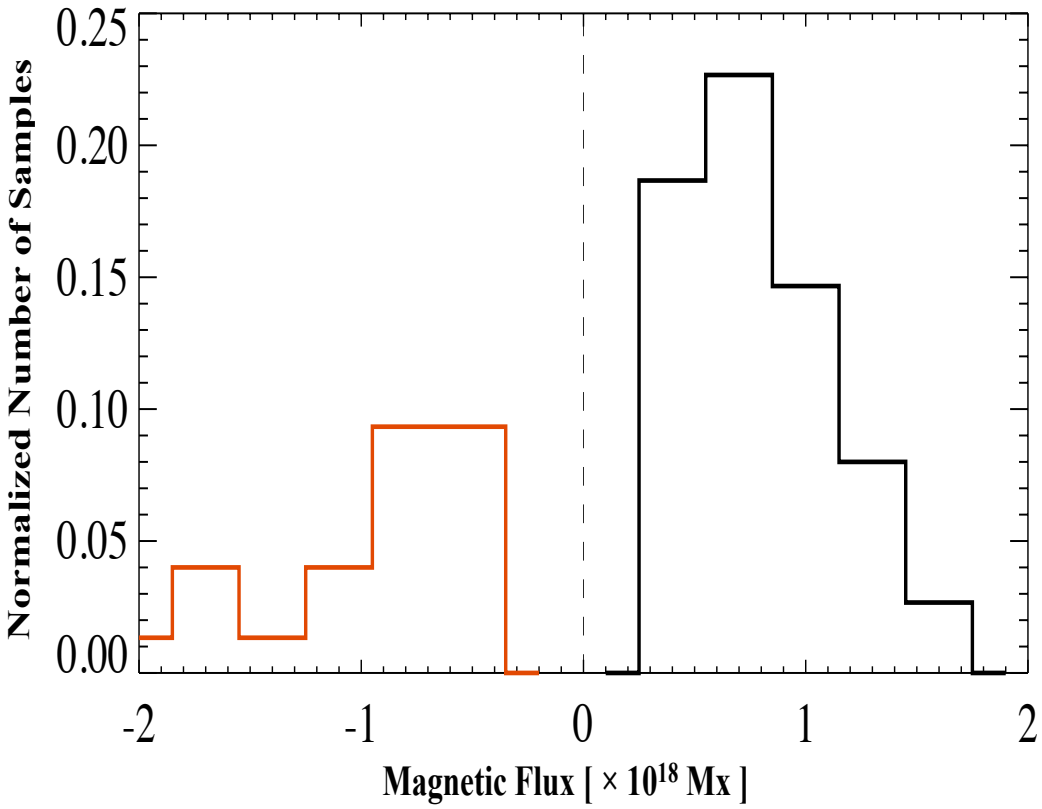

Figure 3.4: Histogram of time-averaged magnetic flux of the 75 samples chosen for this study. Distribution of negative polarity patches (minority polarity) is plotted in red color and positive polarity patches (majority polarity) in black color.

3.3.2 Appearance of Faculae within Magnetic Patches

To find out the coincidence of faculae location with other parameters like magnetic field strength, zenith angle, velocity and filling factor within the magnetic patch, all the sample magnetic patches which enclose facula were selected. The LOS velocity within the magnetic patch is determined from zero-crossing of the Stokes V profile. Zero velocity was defined as the average velocity over all the inverted pixels. We made a vertical (north-south) cut along the slit direction within each of the selected patches through their peak facular intensity location and profiles for all the above mentioned parameters along the vertical cut were obtained. An average profile from the individual profiles for each of the parameters is made and is shown in Figure 3.5. The zero position in the x-axis denote the location of the peak intensity of the facula. The profiles show that at the location of the peak intensity, magnetic field peaks, velocity is quite small and is redshifted and the field is more vertical. The filing factor distribution appears to be rather uniform. The non-uniform distribution of the physical parameters within the patch and the fact that magnetic patches enclose localized concentrations of flux might be an indication that a patch is more complex than a single flux tube structure can explain.

To investigate whether any precursor to the facular appearance can be found out from the frame preceding it using the distribution of parameters like field strength, velocity etc. we carried out the following analysis. For the frames with sample patches possessing facula the physical parameters are averaged over the facula pixels. For the patches in the preceding frame which are devoid of facula we performed the average over the magnetic centroid of the patch and its three

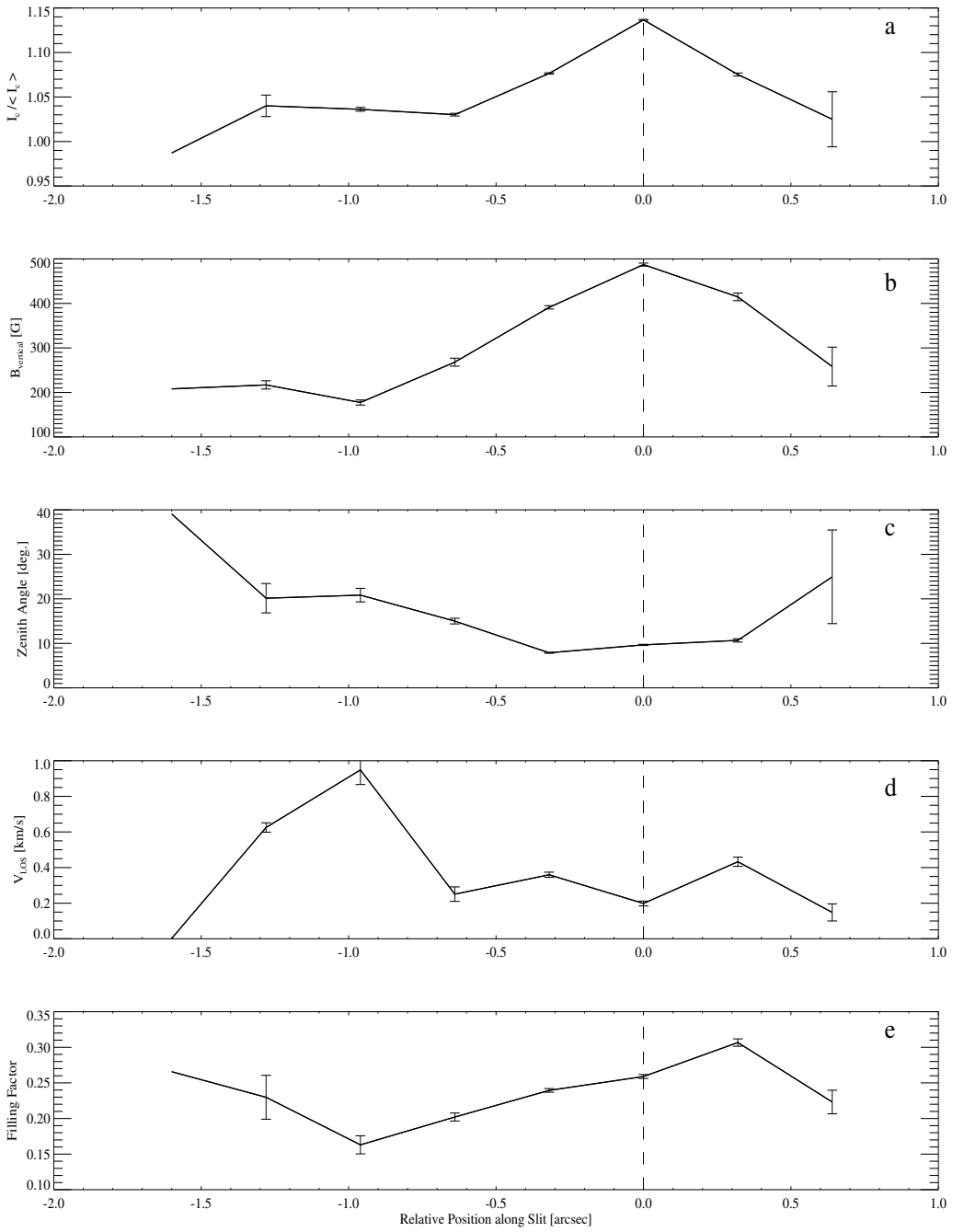

Figure 3.5: The profiles of: (a) normalized intensity, (b) vertical magnetic field, (c) zenith angle ((note that inclination of positive polarity field alone is plotted)), (d) LOS velocity, and (e) filling factor along the slit direction averaged over the samples with facula.

neighboring pixels, assuming that facula appearance occur at the strong field location. Figure 3.6 (a) show that the peak of the intensity distribution increases from about 2% to about 11% of the quiet sun continuum intensity during the interval of 16minutes. The difference in peak field strengths (Fig. 3.6(b)) and inclination (Fig. 3.6(c)) differ only slightly between the two frames during the same interval. The field strength does not show a sudden increase at the time of facula appearance as compared to the intensity. Kaithakkal et al. (2013) reported that the polar facula within magnetic patch exhibit fine structure with a core and an extended halo region. Hence, averaging over the facula region, including both the core and the halo region, within a patch might result in reduced field strength. In the both frames magnetic fields are close to vertical. We does not see any significant difference in horizontal Doppler velocity distributions (Fig. 3.6(d)) between the two frames.

3.3.3 Flow Field at the Time of Appearance and Disappearance of Magnetic Patches

Bisector Analysis

Visual inspection of the magnetograms obtained with the SP observation show unipolar appearance and disappearance of the polar magnetic patches. We investigated whether the photospheric flow field around the patches has any role in the appearance and disappearance of the polar magnetic patches. The variation of the flows with height is also examined by the bisector analysis of the Fe I 630.15 nm line profile. This spectral line is less sensitive to the magnetic field (g = 1.67) in comparison with the Fe I 630.25 nm (g = 2.5) line. Though the magnetic sensitive

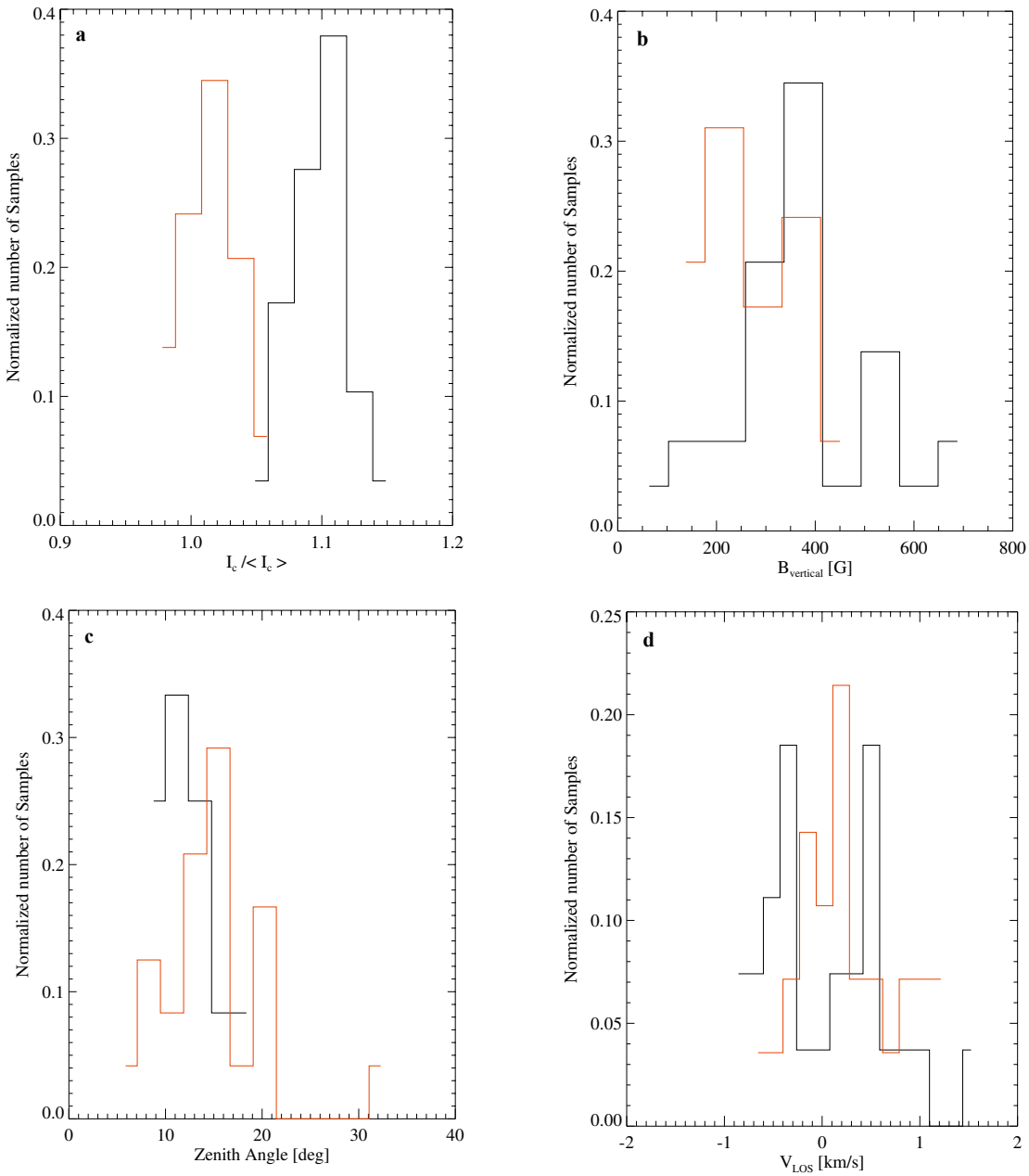

Figure 3.6: Histograms of: (a) normalized intensity, (b) vertical component of the magnetic field strength, (c) zenith angle of the vertical magnetic field (note that inclination of positive polarity field alone is plotted), and (d) LOS Doppler velocity obtained from the Stokes V zero cross point. The histograms in red represent the distribution of parameters within the patch 16 minute before the appearance of the facula and those in black represent the distribution corresponding to the facula pixels.

line is used, the effect of magnetic field on the velocity measurements is assumed to be negligible in the nearly field-free plasma surrounding the magnetic patch. We obtained bisector positions of the line profile at four intensity levels between line core and wing (see Figure 3.7). The formation height decreases with increase in intensity along the line profile. Thus, the bisector level 4, shown in Figure 3.7, forms deeper in the solar photosphere than the bisector level 1. The Doppler velocity is calculated as v = $(\Delta\lambda/\lambda_0)$ c, where λ_0 is 630.15 nm and c is the velocity of light.

The Doppler shift for each bisector level ($\Delta\lambda$) is determined with respect to the reference wavelength position at that level. As we do not have an absolute reference wavelength position, the reference wavelength is determined as follows. For each of the selected sample patch we define a vertical (north-south) slot of height about $96''$ in the slit direction, excluding pixels close to the limb, and width same as that of the patch (defined as the difference between maximum and minimum locations of the patch across the slit direction). The spectral line profiles in this vertical slot were then averaged to obtain a mean spectral line profile. The reference wavelength position for each of the bisector levels was calculated at the respective intensity positions from the mean spectral profile. The reference wavelength position at each bisector level was found to vary by about ± 0.2 pm ($\sim$ 0.1 km/s) between image sequences in which a given patch is present .

Since we are interested in a relative velocity in the region around the magnetic patches, we defined a reference wavelength which gives an average velocity in the region of our interest. In this study, we defined a sub vertical slot of width same as that of the patch and height $\pm 8''$ from the top and bottom boundary respectively of each patch (Figure 3.8). The velocity averaged over this sub slot is defined as

zero velocity in our study.

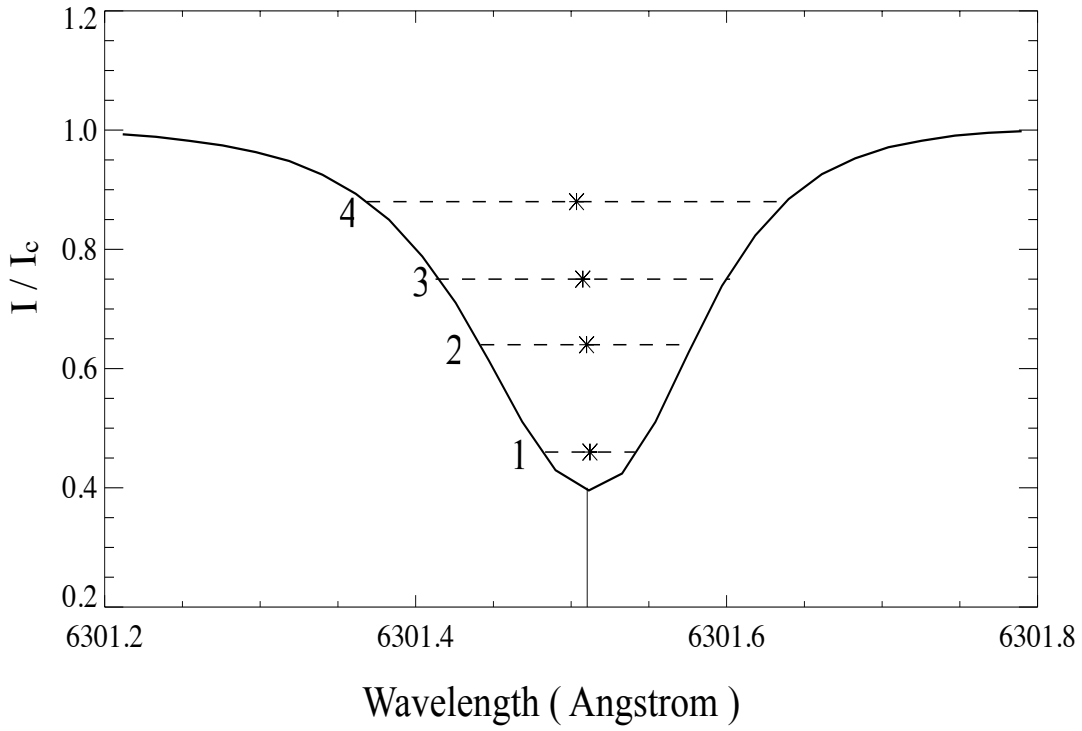

Figure 3.7: Normalized Stokes I profile of the Fe I 6301.5 Å absorption line. The solid vertical line represents the line core position and the asterisks represents the bisector points.

Appearance of Magnetic Patches

In this section we discuss the photospheric flows in and around the 75 magnetic patches during their appearance. We defined t_0 as the time when a magnetic feature is recognized as a patch by the clumping algorithm. The velocity profile in and around the patch along the slit direction is obtained as follows. To minimize the effect of noise, the velocity at each position (within the sub vertical slot) along the slit direction is obtained by averaging the Doppler velocity over the width of

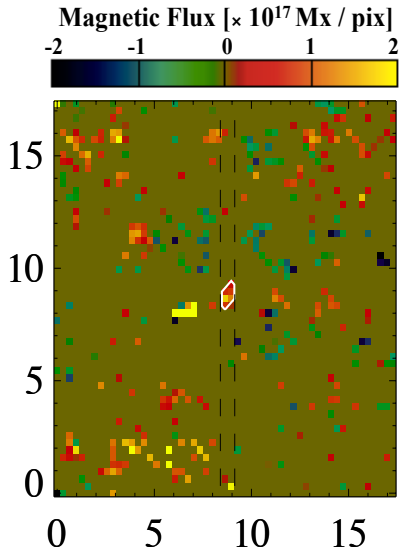

Figure 3.8: Magnetic flux map of a sample patch at time t_0. The solid line encircles the boundary of the patch. The dashed lines mark the edges of the sub vertical slot mentioned in the text. The x and y coordinates are in arcsec.

the sub vertical slot across the slit direction. In general, magnetic patches have a 'ragged' shape and hence have non-uniform width across the patch. So if the width of the patch is smaller than the width of the slot at a given location within the patch, the average is calculated only over those positions within the patch. This separate treatment for the magnetic patch is performed to understand the nature of the flow velocity in the presence of the magnetic field. The zero velocity is subtracted from the Doppler value obtained at each position along the slit. A sample velocity profile at the bisector level 4 at time t_0 is shown in Figure 3.9. The zero position on the x- axis is the location within the patch at which the average intensity becomes maximum. The velocity profile shows dominance of blue shift on the limb-ward side and red shift on the disk center-ward side within a distance of $\pm$ 2″ respectively from the patch boundary. Blue- and red-shifted flows on

the limb- and disk center-ward directions respectively of the patch represent the existence of converging (incoming) flow field. For each patch, we retraced the patch location at time t_0 onto the frame at t_0-16 min (Figure 3.10). Doppler velocity in the sub vertical slot at t_0-16 min is determined using the same method as explained before to examine whether the flow field exhibit any trend prior to the patch appearance around the retraced location. The precursor was not always observed in the magnetograms at t_0-16 min.

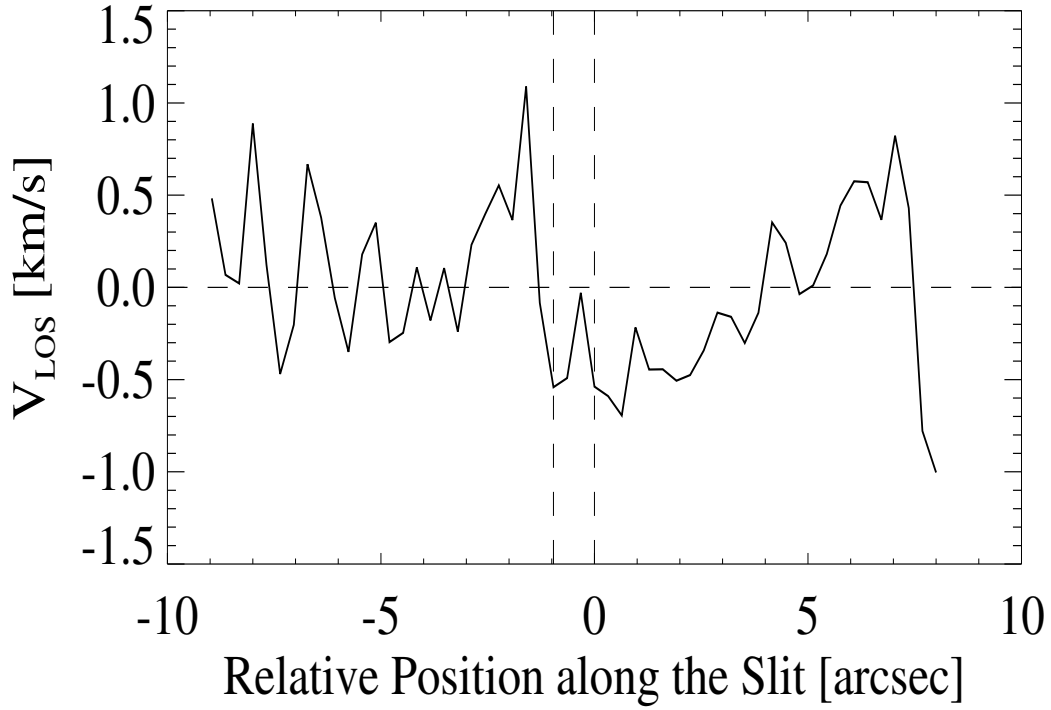

Figure 3.9: The Doppler velocity profile for the magnetic patch shown in Figure 3.8. The position where the average of the normalized intensity becomes maximum within the magnetic patch is defined as 0 in the x axis and the limb is toward right. The vertical dashed lines represent edges of magnetic patch on its limb-ward and disk center-ward side. Positive velocities correspond to flows away from the observer (redshift). The μ value of the magnetic centroid of the patch is 0.31.

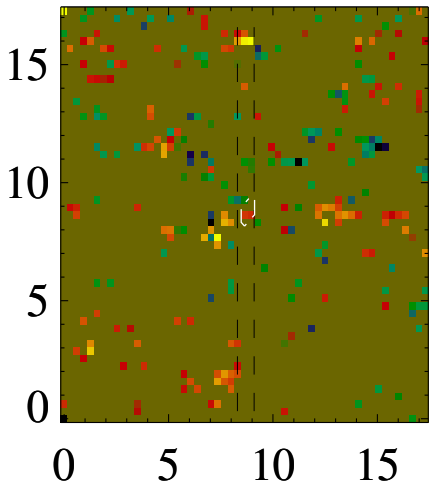

Figure 3.10: The location of the patch in Figure 3.8 is retraced to the frame at t_0-16 min.The dashed contour represents the location of the patch at time t_0.

The above procedure is carried out for all 75 samples to get an average flow field around the retraced patch location at t_0-16 min at the four bisector levels. Figure 3.11 shows weak converging flow around the retraced location of the patch at t_0-16 min. Figure 3.12 show average Doppler profiles for regions within and around patches at time t_0. The plots on the left display that the patch is surrounded by systematic converging flow at all the four bisector levels. The velocity profiles within the patch shows that converging flow continues more or less within the patch. The slight difference in the flow continuity could be due to the difference in two regions: one magnetic and the other nearly non-magnetic. The redshift becomes weaker in the higher layers but the blueshift does not change with height. Considering the patch and its surrounding together, it appears that the horizontal flow is converging to the zero position. The velocity at the zero point is small and is blue-shifted.

The Doppler velocity values on either side of the zero point come from the

region outside the patch. The redshift dominate within a distance of 3″ outside the patch in the disk center direction. Although the extent of the blueshift on the limb side of the patch is not quite clear, it must also be of the same order as the redshift on the disc center-ward side of the patch.

The horizontal dash-dotted lines in Figures 3.11 and 3.12 represent the standard deviation value obtained from the average velocity profile of non-magnetic region. In order to derive this, the spatial mask corresponding to the location of the patch at t_0 was obtained and is shifted randomly across the slit direction such that the region within the mask has zero flux. Then, the Doppler velocity within the sub vertical slot was determined exactly in the same manner as was done with the magnetic patches. This procedure is repeated for all samples and their average Doppler velocity profile as well as its standard deviation which is $\pm$ 0.05 km/sec was obtained. Figure 3.13 show the average profile of the non-magnetic region. The average Doppler velocity profile does not exhibit a systematic flow pattern; it rather shows random variations.

We also calculated average Doppler velocity, at time t_0 -16 min and t_0, over a distance of 3″ from the patch boundary on both the limb- and the disk center-side for each sample. Figure 3.14 shows distribution of the average velocity on the limb- and the disk center-side of the patch separately. The velocity distribution outside the retraced location of the patch at t_0-16 min in the limb ward direction show the existence of an incoming flow toward the patch location, whereas the distribution in the disk ward direction does not exhibit a clear incoming flow. However the histograms show a velocity gradient which indicate the presence of converging flow. The histograms at time t_0 support the existence of converging flow around the patch. Although the dominance of redshift on the disk center side

of the patch is not that evident from the histogram at time t_0, the percentage of samples (specified in the plot) with redshift indicate its prevalence on the disk center-ward direction of the patch.

Inspection of the velocity profiles of the individual samples has shown that not all of them exhibit the converging flow pattern around the patch as shown by the average profile. If the flow field is directed towards the patch from all the directions, the resultant velocity need not always be in a direction favorable to the LOS. This could be one of the reasons for the non-existence of the flow pattern in those samples.

We define the strength of the converging flow field as the difference in peak velocity at the disc center- and the limb-ward side of the patch ($V_\mathrm{r} - V_\mathrm{b}$) within the $3''$ zone around the patch. The variation of strength of the converging flow field with bisector levels is shown in Figure 3.15. The strength of the LOS velocity outside the patch increases as depth increases.

Apparent Death of Magnetic Patches

The time of the final frame in which the magnetic patch is detected with the clumping method is defined as t_f. Figure 3.16 shows two examples of magnetic patches at time t_f and t_f+16 min. The first sample clearly shows the death of the patch via fragmentation, and the second sample seem to be a case of unipolar disappearance. To investigate whether any trend in flow pattern exists during the apparent death of the magnetic patches, the same procedure described in section 3.3.2 was performed for the 75 samples which were born and disappeared during the period of observation. The average velocity profiles at t_f for both the patch and the region surrounding it are shown in Figure 3.17. The profiles on the left side

of the figure show that converging flow exist outside the patches. We found that the converging flow is not continued within the patch and that the flow velocity is redshifted.

The average Doppler velocity, at time t_f, over a distance of $3''$ from the patch boundary on both the limb- and the disk center-side for each sample was determined. Figure 3.18 shows distribution of the average velocity on the limb- and the disk center-side of the patches separately. The histograms display the existence of horizontal incoming flow outside the patch. When compared to velocity distributions at time t_0 (Figure 3.14) the peak of the histograms at time t_f is closer to zero. But this small shift is insignificant compared to the standard deviation of the average velocity of the individual samples ($\sim$ 0.3 km/s). Also we found that the difference in the value of $V_\mathrm{r} - V_\mathrm{b}$ at bisector level 4 between time t_0 and t_f is also small. This indicates that the horizontal converging flow around the patch at time t_f is not weak and might of the same order as that at time t_0.

We also obtained average Doppler velocity profiles at t_f + 16 min, at bisector level 4, for the region surrounding the patch along the slit direction which are shown in Figure 3.19. The profile shows a weak converging flow within a radial distance of $3''$ outside patches. To verify whether a systematic converging flow exist or not, we obtained distribution of average velocity on the limb- and the disk center-side of the patches separately over a distance of $3''$ from the patch boundary. The histograms are shown in Figure 3.20 and the percentage of samples in the distribution is specified in the plot. The distributions show that there is a relative velocity difference between the limb- and disk center ward sides outside of patches which suggests the existence of converging flow at time t_f + 16 min.

The strength of the converging flow, defined by $V_\mathrm{r} - V_\mathrm{b}$ (see section 3.3.3:

Appearance of Magnetic Patches), obtained from the average velocity profiles at t_0 - 16 min, t_0, t_f and t_f + 16 min is given in Table 3.2.

Table 3.2: Variation of Strength of the Converging Flow with Time

Time [min]	$V_r - V_b$ [km/sec]
t_0 - 16	0.37
t_0	0.52
t_f	0.46
t_f+ 16	0.2

The converging flow is strong at time t_0 and t_f and is weakest at time t_f + 16 minute. This indicates that strong converging flow is necessary to form and maintain magnetic patches.

Case Study

The evolution of a sample magnetic patch is shown in this section. Top panel of Figure 3.21 shows the patch evolution in the magnetic flux maps and the bottom panel display the same in normalized continuum intensity maps. The continuum intensity map corresponding to the last detection of the patch (frame 18) shows that a facula is enclosed within the patch and the corresponding magnetic flux map shows that faculae location is cospatial with peak flux location within the patch. The apparent life time of the patch is 32 minutes. The magnetic patch appear to decay via unipolar disappearance. Here we exclude the possibility of

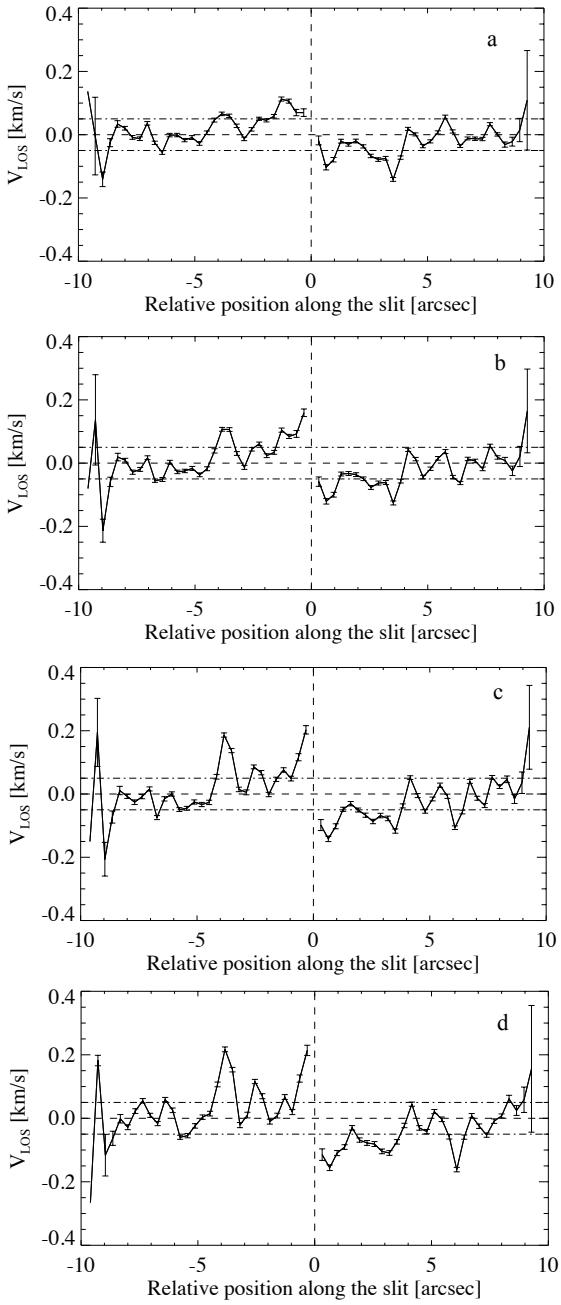

Figure 3.11: The average Doppler velocity profiles at bisector levels: (a) 1, (b) 2, (c) 3, and (d) 4 at time t_0-16 min, from top to bottom. The solid vertical lines represent measured standard errors. The horizontal dash-dotted lines represent ± 1 standard deviation value obtained from the non-magnetic region(see text for details). Limb is towards right. Positive velocities correspond to flows receding from the observer. To obtain this, all velocity profiles from the south polar region are rotated to have the direction of the limb point northward.

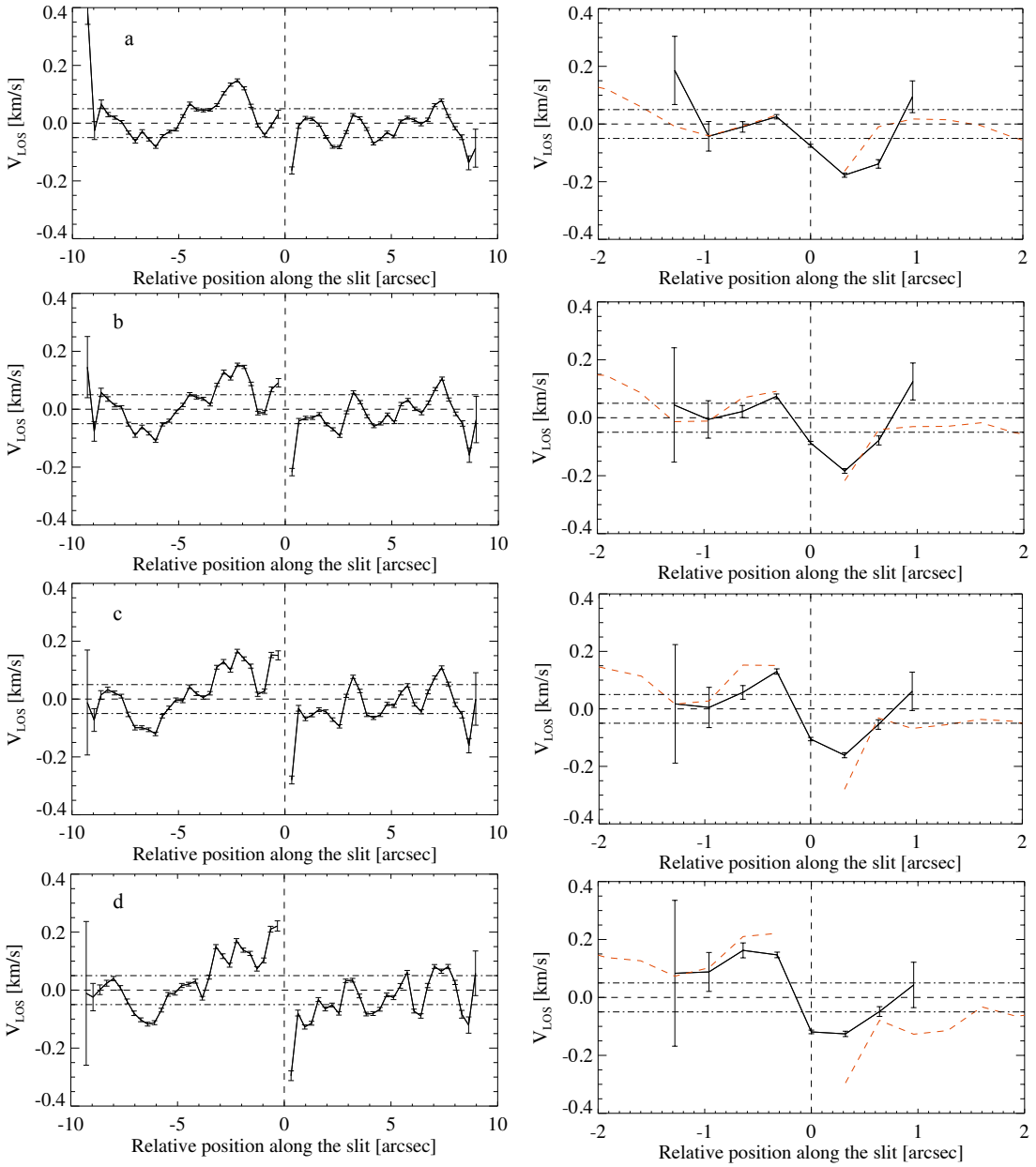

Figure 3.12: The average Doppler velocity profiles at bisector positions: (a) 1, (b) 2, (c) 3, and (d) 4, respectively from top to bottom at time t_0. The plots on the left panel represent horizontal velocity field outside the patch and those on the right represent the velocity field within the patch.

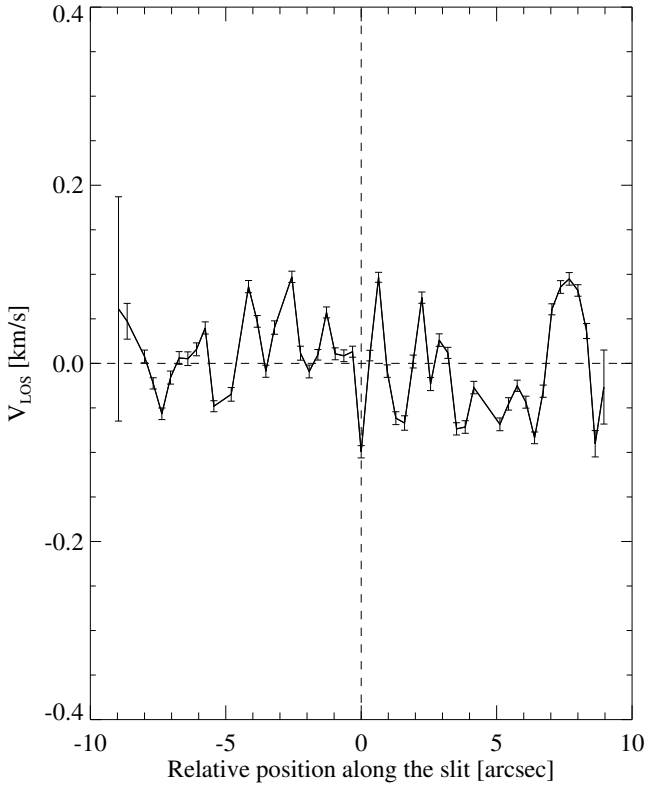

Figure 3.13: The average Doppler velocity profile of the non-magnetic region. Standard error values are represented by the solid vertical lines.

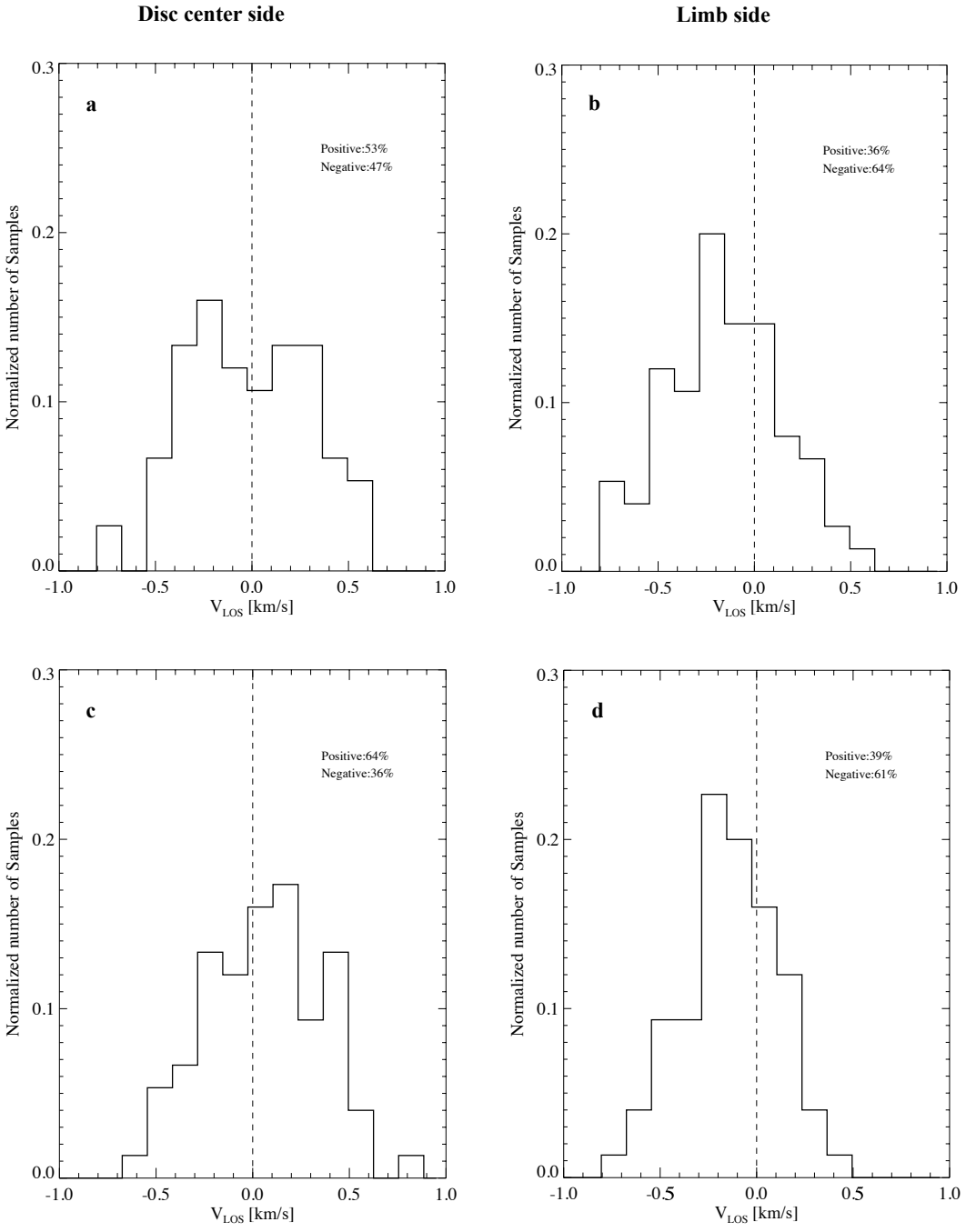

Figure 3.14: Panels a and b represent distribution of average Doppler velocity at time t_0-16 min on the disc center- and limb-side respectively of the patch. Panels c and d are same as a and b respectively, but for timet_0.

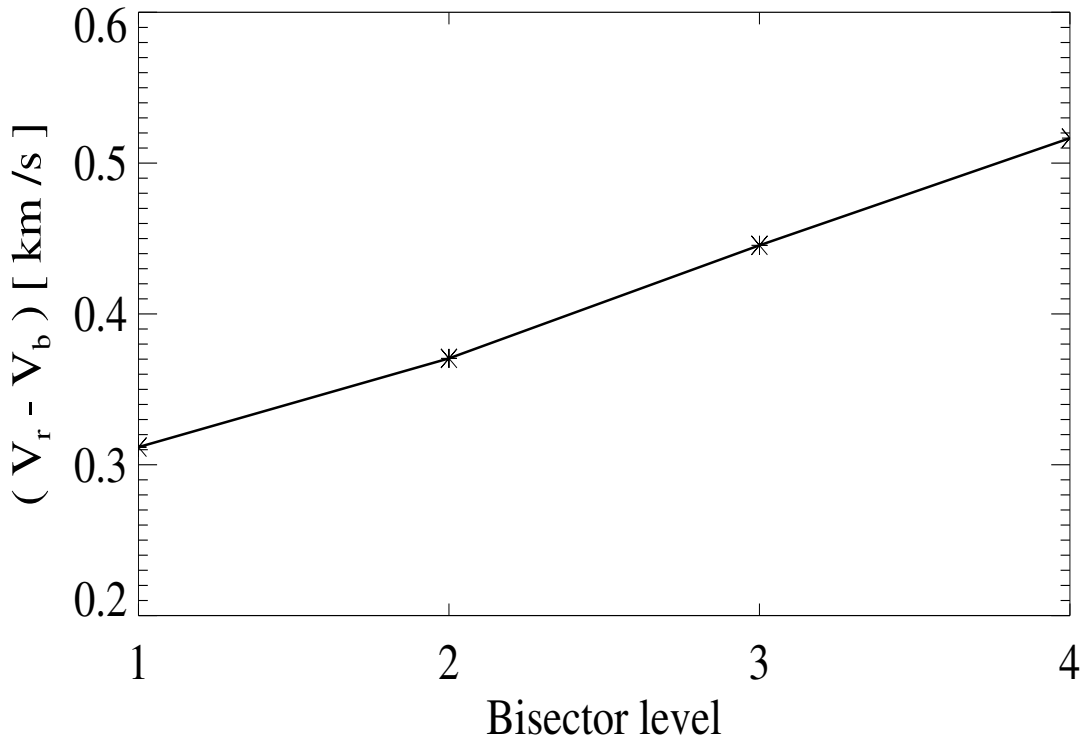

Figure 3.15: The strength of the converging flow as a function of the bisector level.

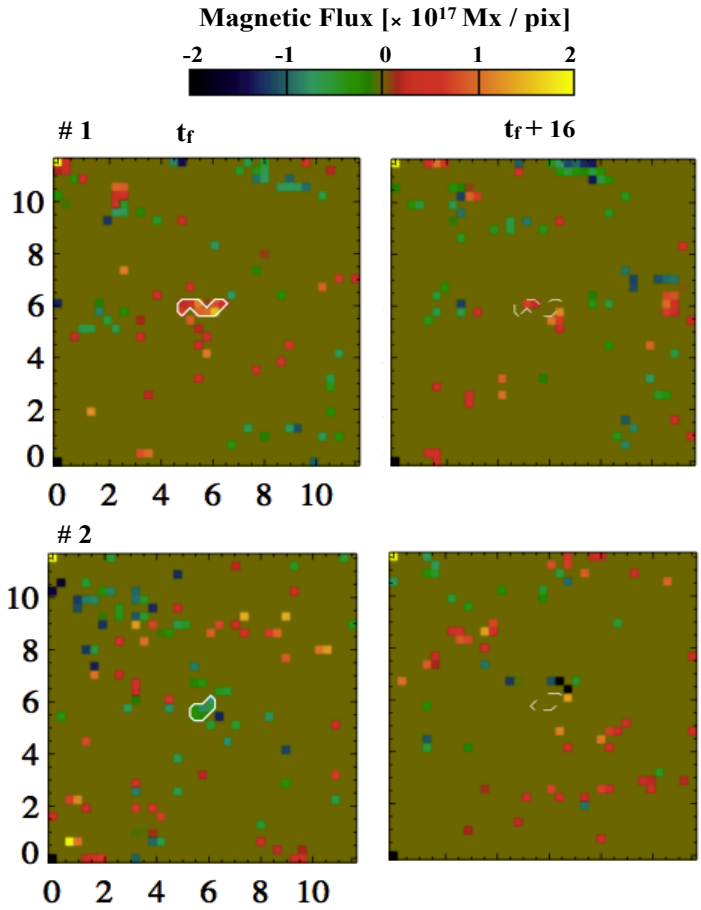

Figure 3.16: Two examples of disappearance of magnetic patches. The upper panels show magnetic flux maps for sample 1 at t_f (left panel) and at t_f + 16 min (right panel). The bottom panels are same but for sample 2.The solid white contour encloses the patch. The dashed contour in right panels represents the spatial location of the patch in the frame at time t_f. The x and y coordinates are in arcsec.

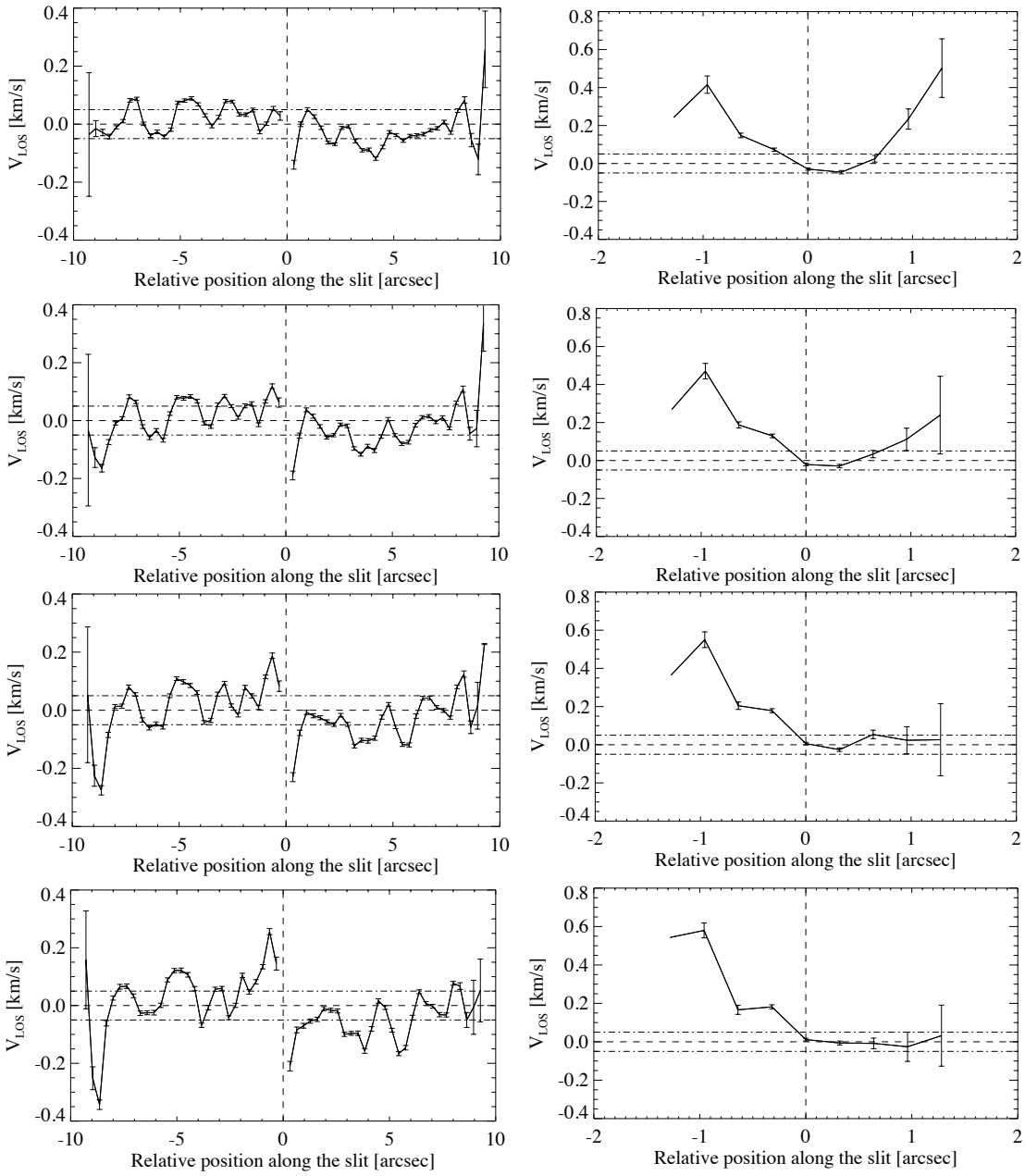

Figure 3.17: Same as Figure 3.12 but for frames at time t_f.

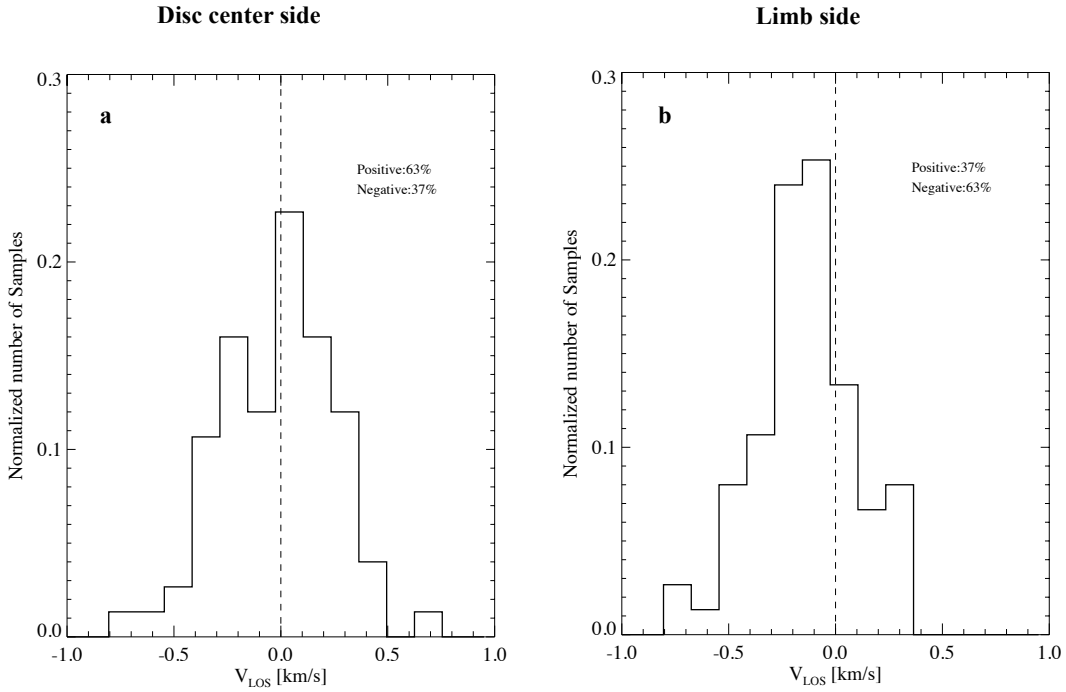

Figure 3.18: Panels a and b represent distribution of average Doppler velocity at time t_f on the disc center- and limb-side respectively of the patch.

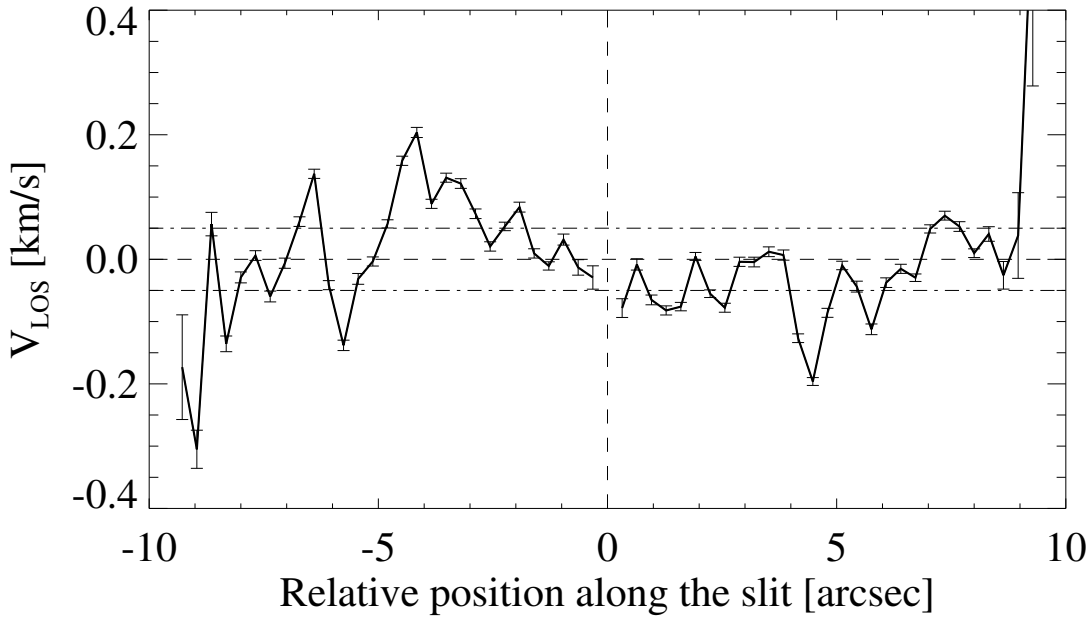

Figure 3.19: The average Doppler velocity profile at bisector level 4 for the frame at time t_f + 16 min.

flux cancellation with an opposite polarity magnetic patch. Firstly, we do not see an opposite polarity magnetic patch in frame 18 in the vicinity of the patch under consideration, and secondly, we do not think it is probable that an opposite polarity patch appear and cancels the existing patch and both disappear completely within a period of 16 minutes such that no trace is left in frame 19.

Figure 3.22 show the variations of magnetic flux and average intensity of the patch with time. The flux evolution display a rising phase and declining phase. The intensity variation shows that peak average intensity is reached when the patch possess facula. Throughout its life time the patch has magnetic flux of the order of 10^{18} Mx. However, we detected facula in only one frame.

The photospheric flow in around the patch during its evolution is shown in Figure 3.23. The profiles from frame 15 through 18 clearly show the existence of

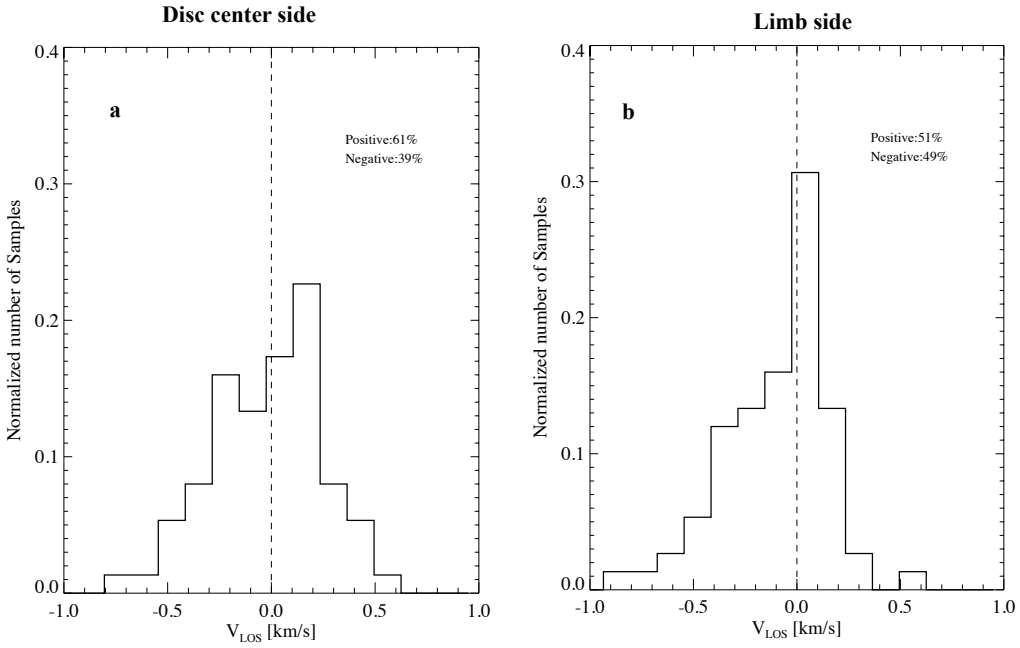

Figure 3.20: Same as figure 3.18 but for time t_f +16 min.

converging flow outside of the patch along the slit direction. The velocity gradient along the slit direction that support convergence is not clear from frame 19. These flow profiles indicate that flow field around individual samples might exhibit a range of variations both in spatial scale and flow strength.

3.4 Summary and Discussion

The average life time of the 75 samples used in this study is about 1h. There are magnetic patches which remained throughout the observation period of 6 hours. To obtain a statistical distribution of life time of the polar magnetic patches, long duration observations are necessary. Liu and Zhao (2009) reported that the life time of polar magnetic elements is longer (16.5 h on average) during solar

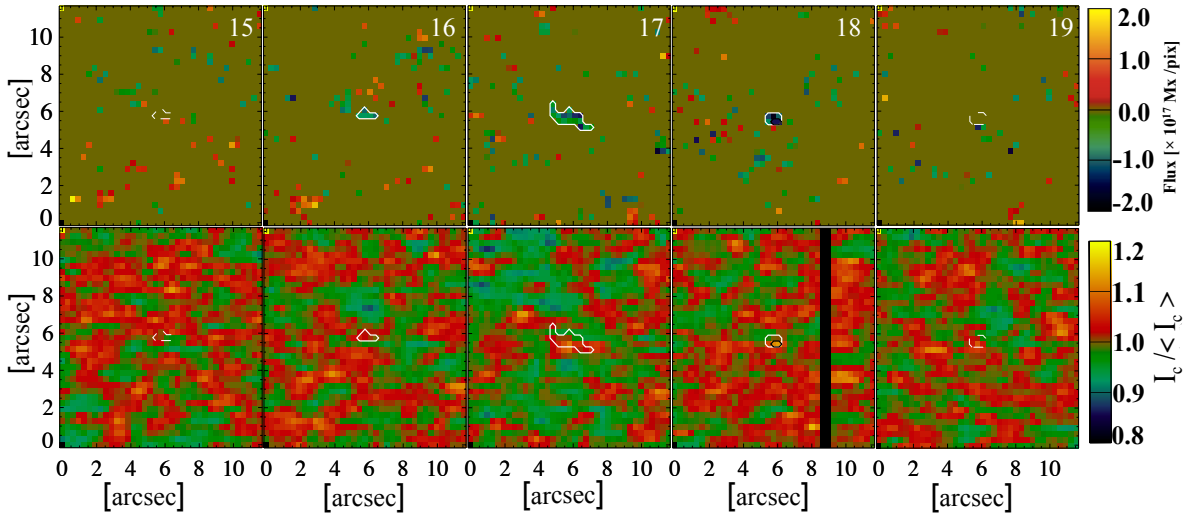

Figure 3.21: Temporal sequence of the magnetic flux maps (top rows) and normalized continuum intensity maps (bottom rows) showing a sample patch evolution (2013 December 11; South pole). White contours outline the patch, and black contour outline facula. The time interval between consecutive frames is 16 min, and the frame numbers are specified on the top right corner of the flux maps.

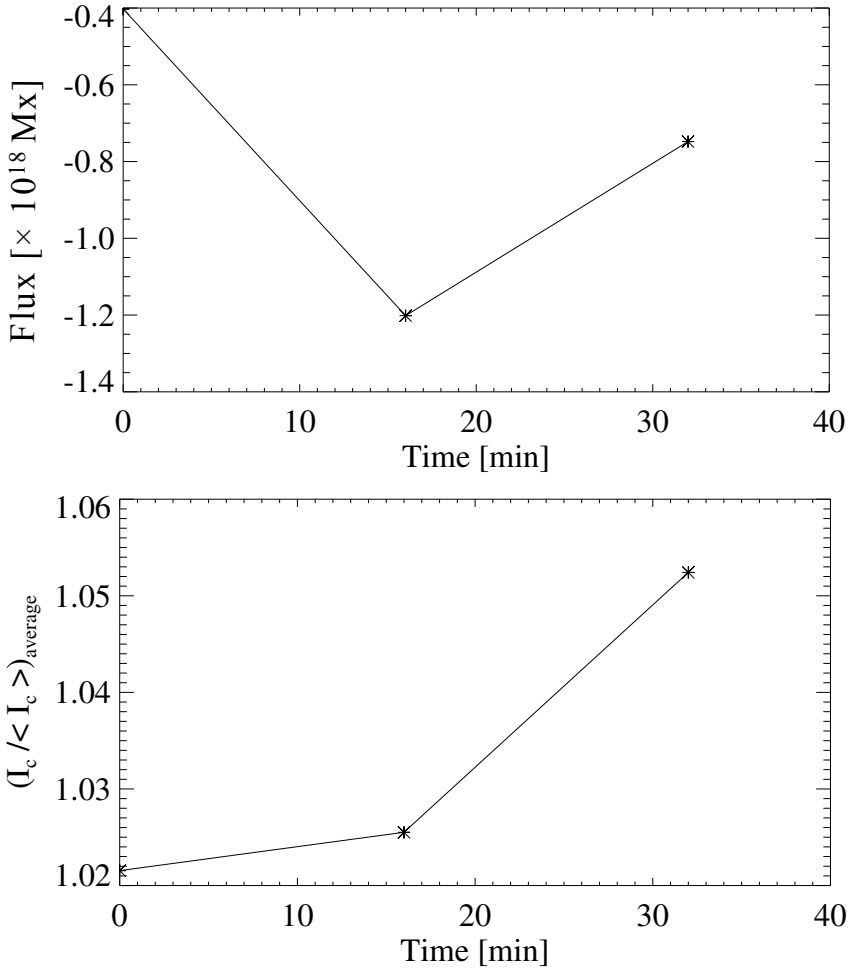

Figure 3.22: Top: variation of patch flux with time. Bottom: variation of average intensity of the patch with time.

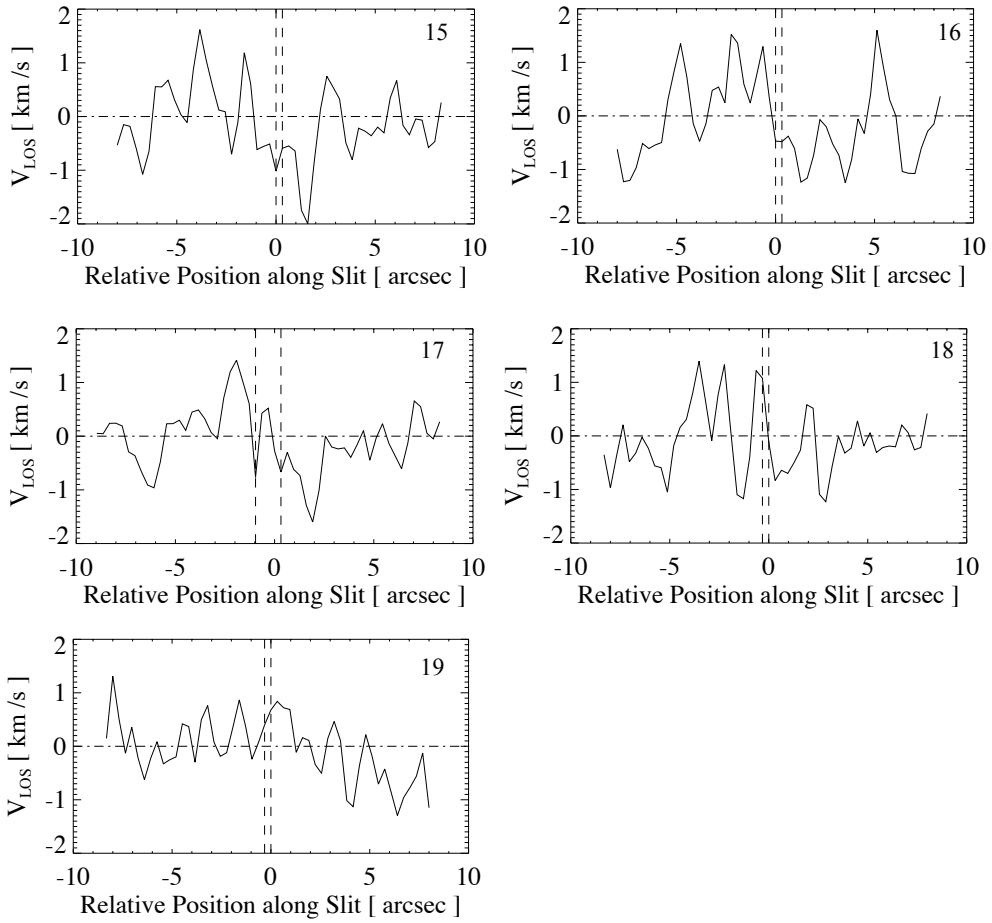

Figure 3.23: LOS Doppler velocity profiles displaying flow field in and around the magnetic patch from timet_0 - 16 min to t_f +16 min. Limb is towards right.

cycle minimum than during cycle maximum (7.3 h). They also found that the dominant polarity elements have longer life time during solar cycle minimum. Our observation corresponds to the solar cycle maximum phase.

We could not identify the precursor to the facula appearance within the patch due to the low time cadence, lack of radial velocity and fine structure information of the facula. To understand the details of the faculae evolution within magnetic patches a high cadence continuous observation is necessary.

This study present the first observation on the role of converging flow on the formation of the polar magnetic patches, whose flux is believed to originate from the decayed active regions. Magnetic patches with life time shorter than 6 hours which satisfy a minimum life time criterion of 32 minutes were considered in this study. The μ value of magnetic centroids of the patches selected for this study fall in the range of 0.3 - 0.2. We found that the polar magnetic patches are surrounded by strong horizontal converging flow during the period of their formation. The converging flow is best represented by the profile at the bisector level 4 which corresponds to a deep photospheric layer. We found, from the average LOS velocity profile at the bisector level 4, that peak of the average converging flow velocity is about 0.2 km/s and that its radius of extent is about $3''$. We also found that the strength of LOS velocity around patches increase as one approaches toward lower photospheric layers, even though the difference in formation height between line core and wing is small.

The mean magnetic flux of the sample patches considered in this study is about 10^{18} Mx. If we consider radius of impact region of the converging flow to be about $10''$ (after foreshortening correction), unit pixel area of $0.32''$ square and a patch flux of 10^{18} Mx then the magnitude of flux per unit pixel would be 0.3×10^{15}

Mx. This calculation indicate that the converging flow we observed is capable of accumulating magnetic flux to form polar patches. We suggest that the isolated 'unipolar appearance' of patches observed in our study most probably occurs due to the coalescence of undetectable flux driven by the converging flow. The above calculations also point to the presence of magnetic flux in the polar region that remain invisible even with high resolution observations from Hinode.

Similar observational studies have been conducted on solar pores, which are magnetic structures with kG field strengths. Keil et al. (1999) observed that pores form at the supergranular cell boundaries by the advection and concentration of magnetic flux driven by the surface flows. Sobotka et al. (1999) reported that the horizontal inflows exist and dominate within a $2''$ zone around pores. Converging flows around pores are also observed by Wang & Zirin (1992) and Sankarasubramanian & Rimmele (2003).

The uniqueness of the LOS Doppler velocity measurements in the polar region is that the measured velocity is dominated by the horizontal component of the photospheric flow field. The LOS Doppler velocity at any position (x, y) on the solar disk is given by: $V(x, y) = V_r(x, y) \cos\theta + V_h(x, y) \sin\theta$, where θ is the heliocentric angle, V_r is the radial and V_h is the horizontal component (along the LOS) of Doppler velocity at (x, y) (Figure 3.18). It should be noted that the measured Doppler values do not include the component of horizontal flow transverse to the LOS. Our study is made under the assumption that the contribution from the horizontal component of radial velocity is minor. However, we think it is possible that the dominance of red-shift within the patch at time t_f (Figure 3.17) is partly contributed by the downdraft within the patch. Assuming that peak down flow speed due to convective collapse is 5 km/s (V_r; Narayan 2011) and that V_h

is negligible during collapse within a magnetic patch, $V(x, y)$ at μ equal to 0.3 is $\sim$ 1.5 km/s. From the average velocity profile within the patch at time t_f peak velocity is about 0.55 km/s ($V(x, y)$), which when corrected for foreshortening (μ = 0.3) gives $\sim$ 1.83 km/s. So even if the downdraft speed is smaller than the peak value mentioned above, its contribution might partially account for the preferential redshift Doppler values observed inside the patch at time t_f.

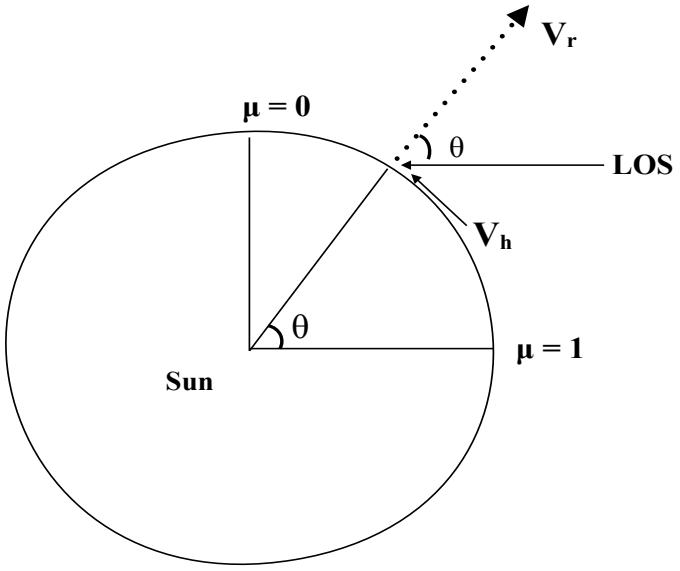

Figure 3.24: Image shows the components of flow velocity observed along the LOS for polar observations.

Spatial scale (after correcting for projection effect) and velocity of the converging flow obtained from the average profile at time t_0, bear resemblance to that of supergranulation. Supergranular flows are known to concentrate magnetic flux as shown by observations close to the disc center (e.g.,Yi & Engvold 1993). The supergranulation exhibits fluctuating cell size, diameters of which vary over a wide range between 20 Mm and 50 Mm with an average horizontal length scale of 32

Mm (Simon & Leighton 1964). There are studies which report supergranule cells of much smaller size, with mean diameters between 10 and 20 Mm (Hagenaar et al. 1997; Berrilli et al. 1999; Srikanth et al. 2000; DeRosa & Toomre 2004). Typical horizontal velocity associated with supergranules is in the range of 300-500 m/s (Simon & Leighton 1964; Shine et al. 2000; Hathaway et al. 2002;); Shine et al. (2000) also showed that some supergranules are associated with horizontal velocity as high as 1km/s. However, in terms of dynamic evolution and shorter life-time of the magnetic patches we obtained, it could be possible that a meso-scale flow also is acting on the magnetic patches that influence the local-scale dynamics of the patches.

We also found that horizontal converging flow exist outside of the patches at the time of their apparent disintegration. Visual inspection of the samples has shown that some of the magnetic patches die by fragmentation and some others disappear in isolation (so called 'unipolar disappearance'). It could be possible that in the case of unipolar disappearance, the magnetic patches underwent fragmentation with the fragments having flux below the detection limit of the instrument, thus rendering them invisible. The physical mechanism causing the 'unipolar disappearance' could be one of the possible methods that leads to the reversal of the polar magnetic field. There must be cancellation between opposite polarity magnetic flux fragments happening eventually, at scales invisible to the spatial resolution of Hinode. It would be interesting to obtain the frequency of occurrence of mechanisms, other than direct cancellation with opposite polarity magnetic flux transported from the active latitudes, by which patches decay.

In summary, the patch evolution seems to include three stages, namely, a) the concentration of the flux fragments by the converging flow field; b) localized con-

centration of magnetic field which is cospatial with facula; and c) the disintegration of the magnetic patch into like polarity fragments (see the cartoon below).

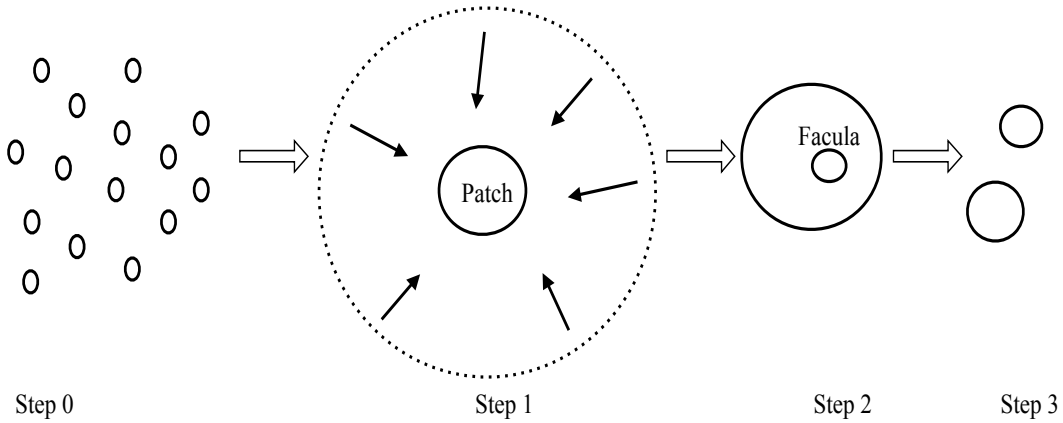

Figure 3.25: The cartoon showing the evolution of the polar magnetic patch.

After Step 3, the magnetic fragments may either coalesce resulting in patch formation or cancel out with opposite polarity fragments. Depending on the phase of the solar cycle one process might dominate over the other; during solar cycle minimum patch formation could be dominating and around cycle maximum cancellation with incoming opposite polarity fragments could be the dominating process.

The case studies show that the converging flow persists outside of the patch throughout its life time. We also found that not all the patches with magnetic flux of about 10^{18} Mx possess facula. Depending on the time of observation we may or may not detect the faculae even if the patch possess enough flux. As mentioned in Kaithakkal et al. (2013) observation time could be one of the factors that plays a role in spotting facula inside a patch. One possibility for the time dependence of facula appearance could be the buffeting of magnetic patches by surrounding

plasma causing temporal flux rearrangement of the patch.

Chapter 4

Concluding Remarks

4.1 Summary

Comprehending the evolution and characteristics of polar magnetic patches is important to obtain a deeper insight into the generation of solar magnetism and its cyclic variation. It is the ensemble of this individual patches that contribute to the global scale behavior of the polar magnetic fields. The major goal of this thesis has been to study the characteristic properties of the polar magnetic patches, their evolution on local scale and their interaction with the plasma motions. It is important to understand the interaction between photospheric plasma motion and polar magnetic field as it contributes largely to the dynamic activities occurring in the chromosphere and corona.

We uncovered the spatial fine structure of the polar patches and their relation to polar faculae. The distribution of intensity, local zenith angle and strength of

the magnetic field vector is found to be non-homogenous within the patch. Our study shows that polar faculae are enclosed within most of the polar patches with flux $\geq 10^{18}$ Mx and are spatially well correlated with peak flux locations within their parent patches. Shiota et al. (2012) observed that it is the unipolar patches of dominant polarity possessing magnetic flux in excess of 10^{18} Mx, that take part in the solar cycle. So our study support the usage of polar faculae as the proxy for the polar magnetic flux. We also found that polar faculae are smaller in size in comparison with their parent patches which implies that contribution of faculae to the polar flux must be smaller in general.

Magnetic field associated with facula region is identified to be more strong and vertical compared to that outside the facula region but within the patch. We speculate that the coexistence of strong and weak field regions within a magnetic patch could be an indication of existence of multiple flux tubes.

We also studied the interaction of photospheric flow field with the polar magnetic patches. This is the first study which present observational result on the role of plasma flows in the formation and evolution of the polar magnetic patches. The magnetic patches are surrounded by strong converging flow during their apparent life time. The converging flow around the patch boundary is best observed in the LOS Doppler velocity profile close to the photosphere. From the average velocity profile obtained at time t_0, the radius of impact of the converging flow is about $3''$ and peak velocity is about 0.2 km/s. Based on our analysis we suggest that the magnetic flux fragments in the polar region are advected and clustered by photospheric converging flows thereby resulting in the formation of polar magnetic patches. Further, we think that the fine structure of polar patches, like the localized strong field regions inside them, must be driven by local mechanisms; for

e.g., convective collapse. Formation of magnetic structures by transportation and accumulation of magnetic flux by converging horizontal flows are also observed in the low-latitude region. The converging flow observed around polar patches appears to be similar to that observed in the low-latitude network region.

Our observations show that, in addition to direct cancellation magnetic patches decay by fragmentation followed by unipolar disappearance or unipolar disappearance without fragmentation. It is possible that the magnetic patches of existing polarity fragment or diffuse away into smaller elements and eventually cancel out with opposite polarity fragments that reach the polar region around solar cycle maximum. So the above mentioned process could be one of the possible mechanisms by which the existing polarity decay during the reversal of the polar magnetic field.

Ito et al. (2010) reported, using Hinode observations obtained during solar cycle minimum, that distribution of vertical magnetic flux in the polar region is asymmetric compared to that in the low-latitude quiet Sun: i.e., magnetic patches of one polarity dominate over the other in the polar region. Though unipolar patches exist (Iida 2012, Lamb et al. 2010) in the low-latitude quiet Sun as well, the probability of cancellation between the opposite polarity patches is high due to the balanced flux distribution. While, in the polar region, imbalance in the flux distribution leads to the dominance of unipolar patches of one polarity. Unipolar patches exist both in the higher and lower latitude regions. Furthermore, in both regions magnetic flux is found to be concentrated by converging flows. We speculate that irrespective of latitude characteristics of individual magnetic patches are determined locally and in that sense patches in the polar region and low-latitude quite Sun region could be similar. And we think that magnetic flux density varia-

tion with latitude and imbalance in the vertical flux distribution, within the polar cap region could be two of the reasons that make polar region different from the quiet Sun region in the lower latitudes.

4.2 Future Work

1) We found that faculae flux account for less than 20% of the total flux from the large flux concentrations examined in our study. This implies that facula flux alone cannot account for the magnetic flux from the polar region. It would be interesting to study in future if there exists any variation in the contribution of facula to the polar flux with the solar activity cycle.

2) The contrast of active region faculae is observed to depend on magnetic field strength and μ value (e.g., Yeo et al. 2013; Ortiz et al. 2002). These studies report that the faculae contrast peaks between $\mu = 0.5$ and $\mu = 0.2$, depending on the field strength, and then decrease towards the extreme limb. The normalized intensity of polar facula pixels decreases steadily from $\mu = 0.4$ to ~ 0.1. We think there exists a $\mu_{\max}$ until which the faculae intensity steadily increases in the case of oblique observations and beyond that value the brightness decreases since one observe less and less of the hot wall of flux tube as μ increases. However it is worth investigating whether the facula brightness depend on any parameter other than the field strength and the μ value, for e.g., latitude. Whether there exist any difference between the active region faculae and polar faculae is a topic that is yet to be investigated.

3) To understand: a) the role of photospheric plasma flows in the rearrangement and related dynamics of the polar patches, b) the mechanism that leads to the

formation of faculae within the patches, and c) reversal of polarity of the polar region a continuous observation with high spatio-temporal resolution is necessary.

References

Babcock, H. D. 1959, ApJ, 130, 364

Babcock, H. W. 1961, ApJ, 133, 572

Blanco Rodríguez, J., Okunev, O. V., Puschmann, K. G., Kneer, F., & Sánchez-Andrade Nuño, B. 2007, A&A, 474, 251

Benevolenskaya, E. E. 1996, Sol. Phys., 167, 47

Benevolenskaya, E. E. 2007, Astron. Nachr., 328, 10

Berger, T. E., Lofdahl, M. G., Shine, R. S., & Title, A. M. 1998, ApJ, 495, 973

Berrilli, F., Ermolli, I., Florio, A., & Pietropaolo, E. 1999, A&A, 344, 965

Charbonneau, P. 2010, Liv. Rev. Sol. Phys., 7, 3

Choudhuri, A. R., Chatterjee, P., & Jiang, J., 2007, Phys. Rev. Lett., 98, 131103

Deng, L. H., Song, J. Y., Xiang, Y. Y., & Tang, Y. K. 2011, JApA, 32, 401

De Rosa, M. L., & Toomre, J. 2004, ApJ, 616, 1242

de Wijn, A. G., Lites, B. W., Berger, T. E., Frank, Z. A., Tarbell, T. D., & Ishikawa, R. 2008, ApJ, 684, 1469

Fisk, L. A., & Schwadron, N. A. 2001, ApJ, 560, 425

Foukal, P., Bernasconi, P., Eaton, H., & Rust, D. 2004, ApJ, 611, L57

Gopalswamy, N., Lara, A., Yashiro, S., & Howard, R. A. 2003, ApJ, 598, L63

Hagenaar, H. J., Schrijver, C. J., & Title, A. M. 1997, ApJ, 481, 988

Hathaway, D. H., Beck, J. G., Han, S., & Raymond, J. 2002, Sol. Phys., 205, 25

Harvey, K., & Recely, F. 2002, Sol. Phys., 211, 31

Harvey, J. W., Branston, D., Henney, C. J., & Keller, C. U. 2007, ApJ, 659, L177

Homann, T., Kneer, F., & Makarov, V. 1997, Sol. Phys., 175, 81

Hyder, C. L. 1965, ApJ, 141, 272

Ichimoto, K., Lites, B., Elmore, D., et al. 2008, Sol. Phys., 249, 233

Iida, Y. 2012, PhD thesis, Univ. of Tokyo

Ito, H., Tsuneta, S., Shiota, D., Tokumaru, M., & Fujiki, K. 2010, ApJ, 719, 131

Kaithakkal, A. J., Suematsu, Y., Kubo, M., Shiota, D., & Tsuneta, S. 2013, ApJ, 776, 122

Keil, S. L., Balasubramaniam, K. S., Smaldone, L. A., & Reger, B. 1999, ApJ, 510, 422

Kosugi, T., Matsuzaki, K., Sakao, T., et al. 2007, Sol. Phys., 243, 3

Lamb, D. A., DeForest, C. E., Hagenaar, H. J., Parnell, C. E., & Welsch, B. T. 2010, ApJ, 720, 1405

Leighton, R. B. 1964, ApJ, 140, 1547

Leighton, R. B. 1969, ApJ, 156, 1

Lites, B. W., Akin, D. L., Card, G., et al. 2013, Sol. Phys., 283, 579

Lites, B. W., Ichimoto, K., 2013, Sol. Phys., 283, 601

Liu, Y., Zhao, J. 2009, Sol. Phys., 260, 289

Makarov, V. I., Sivaraman, K. R. 1986, BASI, 14, 163

Makarov, V. I., & Sivaraman, K. R. 1989, Sol. Phys., 123, 367

Makarov, V. I., & Makarova, V. V. 1996, Sol. Phys., 163, 267

Makarov, V. I., Tlatov, A. G., Sivaraman, K. R. 2001, Sol. Phys., 202, 11

Mordvinov, A. V., & Yazev, S. A. 2014, Sol. Phys., 289, 1971

Muñoz-Jaramillo, A., Sheeley, N. R., Jr, Zhang, J., & DeLuca, E. E. 2012, ApJ, 753, 146

Narayan, G. 2011, A&A, 529, A79

November, L. J., Toomre, J., Gebbie, K. B., & Simon, G. W. 1981, ApJ, 245, L123

Okunev, O. V., & Kneer, F. 2004, A&A, 425, 321

Orozco Suárez, D., & del Toro Iniesta, J. C. 2007, A&A, 462, 1137

Orozco Suárez, D., et al. 2007, PASJ, 59, S837

Ortiz, A., Solanki, S. K., Domingo, V., Fligge, M., & Sanahuja, B. 2002, A&A, 388, 1036

Parker, E. N. 1978, ApJ, 221, 368

Pierce, A. K., Slaughter, C. D., & Weinberger, D. 1977, Sol. Phys., 52, 179

Raouafi, N. E., Harvey, J. W., & Henney, C. J. 2007, ApJ, 669, 636

Roudier, T., Rieutord, M., Brito, D., Rincon, F., Malherbe, J. M., Meunier, N., Berger, T., & Frank, Z. 2009, A&A, 495, 945

Saito, K., & Tanaka, Y. 1960, PASJ, 12, 556

Sankarasubramanian, K., & Rimmele, T. 2003, ApJ, 598, 689

Schatten, K. H., Scherrer, P. H., Svalgaard, L., Wilcox, J. M., 1978, Geophys. Res. Lett., 5, 411

Sheeley, N. R., Jr. 2005, Living Rev. Solar Phys., 2, 5, URL: http://www.livingreviews.org/2005-5 (cited on 30 June 2014)

Sheeley, N. R., Jr. 2008, ApJ, 680, 1553

Shimizu, T., Nagata, S., Tsuneta, S., et al. 2008, Sol. Phys., 249, 221

Shine, R. A., Simon, G. W., & Hurlburt, N. E. 2000, Sol. Phys, 193, 313

Shiota, D., Tsuneta, S., Shimojo, M., et al. 2012, ApJ, 753, 157

Simon, G. W., & Leighton, R. B. 1964, ApJ, 140, 1120

Solanki, S. K., Zufferey, D., Lin, H., Rüedi, I., & Kuhn, J. R. 1996, A&A, 310, L33

Sobotka, M., Vazquez, M., Bonet, J. A., Hanslmeier, A., & Hirzberger, J. 1999, ApJ, 511, 436

Spruit, H. C. 1976, Sol. Phys., 50, 269

Spruit, H. C. 1979, Sol. Phys., 61, 363

Srikanth, R., Singh, J., & Raju, K. P. 2000, ApJ, 534, 1008

Suematsu, Y., Tsuneta, S., Ichimoto, K., et al. 2008, Sol. Phys., 249, 197

Svalgaard, L., Duvall, T. L., Jr., & Scherrer, P. H. 1978, Sol. Phys., 58, 225

Svalgaard, L., & Kamide, Y. 2013, ApJ, 763, 23

Temmer, M., Rybak, J., Bendik, P., Veronig, A., Vogler, F. 2006, A&A, 447, 735.

Tsuneta, S., Ichimoto, K., Katsukawa, Y., et al. 2008a, ApJ, 688, 1374

Tsuneta, S., Ichimoto, K., Katsukawa, Y., et al. 2008b, Sol. Phys., 249, 167

Varsik, J., Wilson, P. R., & Li, Y. 1999, Sol. Phys., 184, 223

Venkatakrishnan, P. 1986, Nature, 322, 156

Waldmeier, M. 1981, SoPh, 70, 251

Wang, Y.-M., Nash, A. G., & Sheeley, N. R., Jr. 1989, ApJ, 347, 529

Wang, H., & Zirin, H. 1992, Sol. Phys., 140, 41

Yeo, K. L., Solanki, S. K., & Krivova, N. A. 2013, A&A, 550, A95

Yi, Z., & Engvold, O. 1993, Sol. Phys., 144, 1

Zolotova, N. V., & Ponyavin, D. I. 2013, Ge&Ae, 53, 945